Draft version March 28, 2017
Typeset using LaTeX **twocolumn** style in AASTeX61

arXiv:1703.09052v1 [astro-ph.HE] 27 Mar 2017

THE PROPERTIES OF GRB 120923A AT A SPECTROSCOPIC REDSHIFT OF $z \approx 7.8$

N. R. Tanvir,[1] T. Laskar,[2,3] A. J. Levan,[4] D. A. Perley,[5] J. Zabl,[6] J. P. U. Fynbo,[6] J. Rhoads,[7] S. B. Cenko,[8,9] J. Greiner,[10,11] K. Wiersema,[1] J. Hjorth,[6] A. Cucchiara,[12] E. Berger,[13] M. N. Bremer,[14] Z. Cano,[15] B. E. Cobb,[16] S. Covino,[17] V. D'Elia,[18,19] W. Fong,[20] A. S. Fruchter,[21] P. Goldoni,[22] F. Hammer,[23] K. E. Heintz,[24,25] P. Jakobsson,[26] D. A. Kann,[15] L. Kaper,[27] S. Klose,[28] F. Knust,[29] T. Krühler,[29] D. Malesani,[6,30] K. Misra,[31] A. Nicuesa Guelbenzu,[28] G. Pugliese,[27] R. Sánchez-Ramírez,[15] S. Schulze,[32] E. R. Stanway,[33] A. de Ugarte Postigo,[15,6] D. Watson,[6] R. A. M. J. Wijers,[27] and D. Xu[34]

[1] *Department of Physics and Astronomy, University of Leicester, University Road, Leicester, LE1 7RH, UK*
[2] *National Radio Astronomy Observatory, 520 Edgemont Road, Charlottesville, VA 22903, USA*
[3] *Department of Astronomy, University of California, 501 Campbell Hall, Berkeley, CA 94720-3411, USA*
[4] *Department of Physics, University of Warwick, Coventry, CV4 7AL, UK*
[5] *Astrophysics Research Institute, Liverpool John Moores University, IC2, Liverpool Science Park, 146 Brownlow Hill, Liverpool, L3 5RF, UK*
[6] *Dark Cosmology Centre, Niels Bohr Institute, Copenhagen University, Juliane Maries Vej 30, 2100 Copenhagen Ø, Denmark*
[7] *School of Earth and Space Exploration, Arizona State University, Tempe, AZ 85287, USA*
[8] *Astrophysics Science Division, NASA Goddard Space Flight Center, 8800 Greenbelt Road, Greenbelt, MD 20771*
[9] *Joint Space-Science Institute, University of Maryland, College Park, MD 20742, USA*
[10] *Max-Planck-Institut für Extraterrestrische Physik, Giessenbachstrasse, D-85748 Garching, Germany*
[11] *Excellence Cluster Universe, Technische Universität München, Boltzmannstrasse 2, D-85748, Garching, Germany*
[12] *University of the Virgin Islands, #2 John Brewers Bay, 00802 St Thomas, VI, USA*
[13] *Harvard-Smithsonian Center for Astrophysics, 60 Garden Street, Cambridge, MA 02138, USA*
[14] *H.H. Wills Physics Laboratory, University of Bristol, Tyndall Avenue, Bristol, BS8 1TL, UK.*
[15] *Instituto de Astrofísica de Andalucía (IAA-CSIC), Glorieta de la Astronomía s/n, E-18008, Granada, Spain*
[16] *Department of Physics, The George Washington University, Washington, DC 20052, USA*
[17] *INAF, Osservatorio Astronomico di Brera, Via E. Bianchi 46, I-23807 Merate (LC), Italy*
[18] *INAF-Osservatorio Astronomico di Roma, Via Frascati 33, I-00040 Monteporzio Catone, Italy*
[19] *ASI-Science Data Centre, Via del Politecnico snc, I-00133 Rome, Italy*
[20] *Steward Observatory, University of Arizona, 933 N. Cherry Avenue, Tucson, AZ 85721 USA*
[21] *Space Telescope Science Institute, 3700 San Martin Drive, Baltimore, MD 21218, USA*
[22] *APC, Astroparticule et Cosmologie, Universite Paris Diderot, CNRS/IN2P3, CEA/Irfu, Observatoire de Paris, Sorbonne Paris Cit, 10, Rue Alice Domon et Lonie Duquet, 75205, Paris Cedex 13, France*
[23] *GEPI, Observatoire de Paris, CNRS, 5 Place Jules Janssen, Meudon F-92195, France*
[24] *Centre for Astrophysics and Cosmology, Science Institute, University of Iceland, Dunhagi 5, 107 Reykjavk, Iceland*
[25] *Dark Cosmology Centre, Niels Bohr Institute, University of Copenhagen, Juliane Maries Vej 30, 2100 Copenhagen, Denmark*
[26] *Centre for Astrophysics and Cosmology, Science Institute, University of Iceland, Dunhagi 5, 107, Reykjavik, Iceland*
[27] *Anton Pannekoek Institute for Astronomy, University of Amsterdam, Postbus 94249, NL-1090 GE Amsterdam, the Netherlands*
[28] *Thüringer Landessternwarte Tautenburg, Sternwarte 5, 07778 Tautenburg, Germany*
[29] *Max-Planck-Institut für Extraterrestrische Physik, Giessenbachstrasse, 85748, Garching, Germany*
[30] *DTU Space, National Space Institute, Technical University of Denmark, Elektrovej 327, DK-2800 Lyngby, Denmark*
[31] *Aryabhatta Research Institute of Observational Sciences (ARIES), Manora Peak, Nainital 263 002, India*
[32] *Department of Particle Physics and Astrophysics, Weizmann Institute of Science, Rehovot 7610001, Israel*
[33] *Department of Physics, Gibbet Hill Road, Coventry, CV4 7AL, UK*
[34] *CAS Key Laboratory of Space Astronomy and Technology, National Astronomical Observatories, Chinese Academy of Sciences, Beijing 100012, China*

Corresponding author: N. R. Tanvir
nrt3@leicester.ac.uk

(Received; Revised; Accepted)

Submitted to ApJ

ABSTRACT

Gamma-ray bursts (GRBs) are powerful probes of early stars and galaxies, during and potentially even before the era of reionization. Although the number of GRBs identified at $z \gtrsim 6$ remains small, they provide a unique window on typical star-forming galaxies at that time, and thus are complementary to deep field observations. We report the identification of the optical drop-out afterglow of *Swift* GRB 120923A in near-infrared Gemini-North imaging, and derive a redshift of $z = 7.84^{+0.06}_{-0.12}$ from VLT/X-shooter spectroscopy. At this redshift the peak 15-150 keV luminosity of the burst was $3.2 \times 10^{52}\,{\rm erg\,s^{-1}}$, and in fact the burst was close to the *Swift*/BAT detection threshold. The X-ray and near-infrared afterglow were also faint, and in this sense it was a rather typical long-duration GRB in terms of rest-frame luminosity. We present ground- and space-based follow-up observations spanning from X-ray to radio, and find that a standard external shock model with a constant-density circumburst environment with density, $n \approx 4 \times 10^{-2}\,{\rm cm^{-3}}$ gives a good fit to the data. The near-infrared light curve exhibits a sharp break at $t \approx 3.4$ days in the observer frame, which if interpreted as being due to a jet corresponds to an opening angle of $\theta_{\rm jet} \approx 5$ degrees. The beaming corrected γ-ray energy is then $E_\gamma \approx 2 \times 10^{50}$ erg, while the beaming-corrected kinetic energy is lower, $E_{\rm K} \approx 10^{49}$ erg, suggesting that GRB 120923A was a comparatively low kinetic energy event. We discuss the implications of this event for our understanding of the high-redshift population of GRBs and their identification.

Keywords: gamma-ray burst: individual (GRB 120923A) — gamma-ray burst: general — galaxies: high-redshift — dark ages, reionization, first stars

1. INTRODUCTION

The early galaxies in the universe, born in the first few hundred million years after the Big Bang, have been the focus of extensive observational searches in recent years. The interest is not only in the nature of these primordial collapsed objects, but also in whether the UV light they emitted was sufficient to have brought about the reionization of the intergalactic medium (IGM) (e.g., **?**). Since the recent *Planck* results suggest a peak of the reionization era at $z \sim$8–9 (**?**), the focus on galaxies in the range $z = 7$–10 has become even more intense.

Directly detecting galaxies at such redshifts, however, is highly challenging due to their intrinsic faintness and high luminosity distance; the samples of $z > 8$ galaxies in the *Hubble* Ultra-Deep Field (HUDF) are almost entirely candidates based on photometric redshifts. Furthermore, although Lyman-α emission has now been detected in one galaxy at $z = 8.7$ (Zitrin et al. 2015), the rising neutral hydrogen in the IGM itself increasingly absorbs this emission, which likely contributes to the declining Lyman-α detection rates at $z > 7$ (Bunker et al. 2013; Bolton & Haehnelt 2013). The highest spectroscopic redshifts for galaxies based on the Lyman-α break are $z \approx 7.5$, in the case of a galaxy benefiting from significant amplification by gravitational lensing of a comparatively bright galaxy (Watson et al. 2015), and a surprisingly luminous galaxy recently claimed to be at $z \approx 11.1$ (Oesch et al. 2016).

Long-duration gamma-ray bursts (GRBs) are the most luminous transients known (e.g., Racusin et al. 2008), and are unambiguously linked to the core-collapse of massive stars (e.g., Hjorth et al. 2003; Xu et al. 2013; Maselli et al. 2014). Thus, they provide an alternative tracer of galaxies in the early universe, and indeed are currently the only signature we have of individual stars at such distances. Redshifts can often be measured from afterglow spectroscopy, a method that benefits from their simple underlying power-law continua against which the Lyman-α break imprints an unmistakable signature at high-z. Afterglow spectroscopy also gives information on the metal enrichment in the host galaxies, complementary to measurements of abundances in ancient stars locally (e.g., Frebel & Norris 2015), and the neutral fraction in the surrounding IGM (Barkana & Loeb 2004; Totani et al. 2006; Tanvir & Jakobsson 2007; Thöne et al. 2013; Hartoog et al. 2015; Chornock et al. 2014; Melandri et al. 2015).

The hosts of high redshift GRBs provide a census of primordial star-forming galaxies. It is likely that a large fraction of all star formation at $z > 7$ was occurring in small galaxies too faint to be seen in the HUDF (e.g., Bouwens et al. 2015), and similarly challenging even for the *James Webb Space Telescope* (*JWST*) by $z \sim 10$. Deep searches for high-z GRB hosts can in principle directly constrain this fraction, which is crucial for quantifying the total contribution of galaxies to the reionization budget (see e.g., Tanvir et al. 2012; Trenti et al. 2012; McGuire et al. 2016, for applications of this approach).

Of course, fully exploiting GRBs as high redshift probes also depends on understanding the extent of any evolution of the GRB population as a whole over cosmic time, and whether they preferentially select certain host galaxies or modes of star formation. Recent studies have found evidence that GRBs follow star formation in a fairly unbiased way below a threshold of roughly a third Solar to Solar metallicity (Krühler et al. 2015; Vergani et al. 2015; Perley et al. 2016; Graham & Fruchter 2017), which bodes well for using them as tracers of star formation at high redshift. Other studies have found hints of possible evolution of, for example, shorter rest-frame duration (Littlejohns et al. 2013) and narrower jet opening angle (Laskar et al. 2014), with increasing redshift, although samples remain small and selection effects hard to assess.

To date, the most distant GRBs found have been GRB 090423, with a spectroscopic redshift of $z = 8.2$ (Tanvir et al. 2009; Salvaterra et al. 2009), and GRB 090429B, with a photometric redshift of $z \approx 9.4$ (Cucchiara et al. 2011), although the latter result could be as low as $z \approx 7$ if there is significant dust obscuration in the host. Here we report the discovery of GRB 120923A at a spectroscopic redshift of $z \approx 7.8$, corresponding to an age of the universe of ≈ 670 Myr, and present our modelling of its afterglow.

Throughout the paper, we adopt the following values for cosmological parameters: $H_0 = 71\,\mathrm{km\,s^{-1}\,Mpc^{-1}}$, $\Omega_M = 0.27$ and $\Omega_\Lambda = 0.73$. All times are in the observer frame, uncertainties are at the 68% confidence level (1σ), unless otherwise noted, and magnitudes are in the AB system.

2. OBSERVATIONS

2.1. *Swift observations*

GRB 120923A triggered the *Swift* Burst Alert Telescope (BAT; Barthelmy et al. 2005) on 2012 Sep 23 at 05:16:06 UT (Yershov et al. 2012). The observed burst duration was $T_{90} = 27.2 \pm 3.0$ s, with a fluence of $(3.2 \pm 0.8) \times 10^{-7}\,\mathrm{erg\,cm^{-2}}$ (15–150 keV; Markwardt et al. 2012). The 1-s peak flux was $F_{15-150\,\mathrm{keV}} = 4.1 \times 10^{-8}\,\mathrm{erg\,cm^{-2}\,s^{-1}}$ (Lien et al. 2016), close to the effective detection threshold of BAT. The time-averaged γ-ray spectrum is well fit by a power law with an exponential cut-off, with a photon index of $\Gamma = -0.29 \pm 1.66$

Table 1. GRB 120923A: Log of X-ray observations

$\Delta t_{\rm start}$ (hr)	$\Delta t_{\rm end}$ (hr)	Flux (10^{-12} erg cm^{-2} s^{-1})	Flux density at 1 keV (μJy)
0.042	0.079	7.2 ± 1.6	0.77 ± 0.16
0.079	0.118	6.9 ± 1.5	0.67 ± 0.15
0.118	0.165	6.0 ± 1.3	0.59 ± 0.14
0.165	0.224	4.5 ± 1.0	0.45 ± 0.10
0.224	0.275	4.1 ± 1.0	0.41 ± 0.10
0.275	0.431	2.2 ± 0.4	0.22 ± 0.04
9.78	90.2	0.018 ± 0.006	$(1.8 \pm 0.7) \times 10^{-3}$

NOTE— XRT 0.3–10 keV flux measurements obtained in photon-counting mode. The start and end time of each observation is relative to the BAT trigger time of 2012 Sep 23 05:16:06 (UT). The count rate light curve has been converted to a flux density at 1 keV using a photon index of $\Gamma = 1.77$.

and peak energy, $E_{\rm peak} = 44.4 \pm 10.6$ keV (both at 90% confidence). Integrating the BAT (15–150 keV) spectral model taking $z \approx 8$ (the evidence for a redshift of this order is presented in Section 3), and including the effect of statistical uncertainties in all measured quantities using a Monte Carlo analysis, we find that the isotropic equivalent γ-ray energy is $E_{\gamma,\rm iso} = (4.8^{+6.1}_{-1.6}) \times 10^{52}$ erg (1–10^4 keV, rest frame).

The *Swift* X-ray telescope (XRT; Burrows et al. 2005) began observing the field at 05:18:26.0 UT, 140 s after the BAT trigger, leading to a detection of the X-ray afterglow. The source was localized to RA = $20^{\rm h}15^{\rm m}10\overset{\rm s}{.}73$, Dec=+06°13′16″.9 (J2000), with an uncertainty radius of 1″.9 (90% containment). XRT continued observing the afterglow for 3.6 days in photon-counting (PC) mode, with the last detection at ≈ 0.6 days.

We extracted XRT PC-mode spectra using the on-line tool on the *Swift* website (Evans et al. 2007, 2009)[1]. We used Xspec (v12.8.2) to fit the PC-mode spectrum between 1.7×10^{-3} and 0.67 days, assuming a photoelectrically absorbed power law model (`tbabs` × `pow`) at the redshift of the GRB, and a Galactic neutral hydrogen column density of $N_{\rm H,MW} = 1.5 \times 10^{21}$ cm^{-2} (Willingale et al. 2013). Our best-fit model has a photon index of $\Gamma = 1.77 \pm 0.14$ (68% confidence intervals, estimated using Markov Chain Monte Carlo in Xspec; C-stat= 84 for 105 degrees of freedom). The data do not constrain intrinsic absorption within the host galaxy (see also Starling et al. 2013). In the following analysis, we assume $N_{\rm H,int} = 0$ and use the 0.3–10 keV count rate light curve from the *Swift* website, together with $\Gamma = 1.77$, to compute the 1 keV flux density (Table 1).

2.2. *Ground-based imaging*

We obtained optical and near infra-red (NIR) imaging from Gemini-North using the Near Infrared Imager and Spectrometer (NIRI) and Gemini Multi-Object Spectrograph (GMOS), and the United Kingdom Infra-Red Telescope (UKIRT) using the Wide-Field Camera (WFCAM), beginning 80 min after the *Swift* trigger. Conditions in Hawaii were excellent with $\approx 0\overset{''}{.}5$ full-width-half-maximum (FWHM) seeing, and the target was at low airmass for several hours. We detected a point source in the JHK bands at RA = $20^{\rm h}15^{\rm m}10\overset{\rm s}{.}78$, Dec = +06°13′16″.3 (J2000), accurate to ±0.3″ in each dimension, which is consistent with the X-ray position. The source was absent in the $rizY$ bands (Figure 1), and its blue colour of H-$K \approx 0.1$ mag, together with being a Y-band drop-out ($Y - J \gtrsim 1$ mag), suggested a very high redshift of $z \gtrsim 7$. The NIR counterpart faded in subsequent photometry obtained with the Very Large Telescope (VLT) Infrared Spectrometer and Array Camera (ISAAC), and the European Southern Observatory/Max Planck Gesellschaft (ESO/MPG) 2.2m GRB Optical and Near Infrared Detector (GROND; Greiner et al. 2008), in addition to UKIRT and Gemini-North over the next several nights, confirming it to be the GRB afterglow.

We performed photometry using `Gaia`[2], with the target aperture placed at the location of the afterglow as determined from the high-S/N J-band image and the aperture size set according to the seeing ($\approx 1.3\times$FWHM). We tied the calibration of the WFCAM JHK-band images to the 2MASS photometric system[3] using many stars on each frame, and tied the smaller field NIRI and ISAAC images to this using a secondary sequence of fainter stars close to the burst location. We obtained optical riz-band calibration using the wide-field GROND observations. The Y-band calibration was achieved by interpolating the sequence star magnitudes between z and J according to $Y = J + 0.534(z - J) - 0.058$ (derived from GROND observations of photometric standard stars). Uncertainties introduced by these calibration steps are included in the error budget, but are small compared to the random errors on the afterglow photometry. We summarise our NIR and optical observations and photometry in Table 2 (note, the GROND limits at the afterglow location

[1] http://www.swift.ac.uk/xrt_spectra/00534402

[2] http://astro.dur.ac.uk/$\sim$pdraper/gaia/gaia.html

[3] http://www.ipac.caltech.edu/2mass/releases/allsky/doc/sec6_4a.html

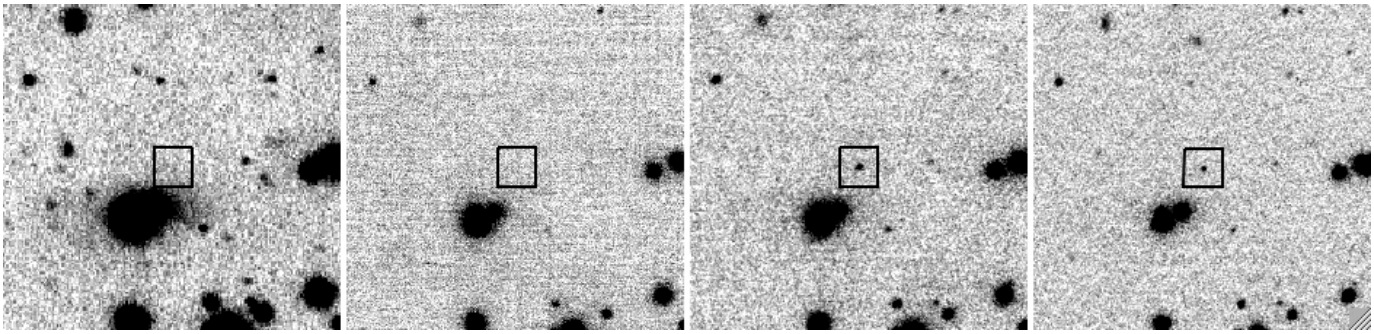

Figure 1. Mosaic of GRB 120923A images obtained with Gemini-North. Panel 1 is $r + i + z$ from GMOS; panel 2 is Y from NIRI; panel 3 is J from NIRI and panel 4 is $H + K$ from NIRI. The inset box is 3 arcsec on a side, and the orientation is north up, east left.

Table 2. GRB 120923A: Log of optical and NIR imaging observations and afterglow photometry

$\Delta t_{\rm start}$(hr)	$\Delta t_{\rm end}$ (hr)	Telescope/Camera	Filter	Exp. (min)	Measured flux (μJy)	AB_0
1.372	1.701	Gemini-N/NIRI	J	17	2.74 ± 0.14	22.69 ± 0.05
1.898	2.050	Gemini-N/NIRI	Y	8	0.21 ± 0.42	> 23.69
3.241	3.396	Gemini-N/NIRI	H	8	2.75 ± 0.23	22.73 ± 0.09
3.442	3.597	Gemini-N/NIRI	K	8	2.80 ± 0.28	22.73 ± 0.10
3.705	4.199	Gemini-N/NIRI	Y	26	0.17 ± 0.23	> 24.26
4.311	4.464	Gemini-N/NIRI	J	8	2.09 ± 0.33	22.99 ± 0.16
23.79	24.14	Gemini-N/NIRI	J	17	1.27 ± 0.39	23.52 ± 0.29
2.164	2.461	Gemini-N/GMOS	r	15	0.014 ± 0.028	> 26.43
2.473	2.769	Gemini-N/GMOS	i	15	0.032 ± 0.031	> 26.20
2.781	3.078	Gemini-N/GMOS	z	15	-0.029 ± 0.150	> 25.05
1.461	1.958	UKIRT/WFCAM	K	24	4.81 ± 0.88	22.15 ± 0.18
2.036	2.538	UKIRT/WFCAM	H	24	3.79 ± 0.51	22.38 ± 0.14
2.565	3.062	UKIRT/WFCAM	J	24	2.38 ± 0.62	22.85 ± 0.25
4.331	4.831	UKIRT/WFCAM	K	24	3.08 ± 1.06	22.63 ± 0.32
4.852	5.225	UKIRT/WFCAM	J	18	2.40 ± 0.83	22.84 ± 0.32
23.66	24.15	UKIRT/WFCAM	H	24	1.16 ± 1.10	> 22.51
18.52	18.87	VLT/ISAAC	$K_{\rm s}$	15	3.55 ± 1.01	22.48 ± 0.27
18.91	19.26	VLT/ISAAC	H	15	2.92 ± 0.88	22.66 ± 0.29
19.31	19.66	VLT/ISAAC	J	15	1.57 ± 0.56	23.30 ± 0.33
67.82	69.25	VLT/ISAAC	J	60	0.71 ± 0.26	24.16 ± 0.34
18.58	20.35	VLT/FORS2	z	80	0.020 ± 0.088	> 25.53
102.2	103.9	*HST*/WFC3-IR	F140W	10	0.21 ± 0.03	25.49 ± 0.12
120.0	127.8	*HST*/WFC3-IR	F140W	25	0.13 ± 0.02	26.02 ± 0.14
156.5	159.8	*HST*/WFC3-IR	F140W	15	0.11 ± 0.02	26.20 ± 0.19
172.5	183.7	*HST*/WFC3-IR	F140W	10	0.072 ± 0.015	26.66 ± 0.21
477.3	479.1	*HST*/WFC3-IR	F140W	43.5	0.014 ± 0.010	> 27.46

NOTE— The start and end time of each observation is relative to the BAT trigger time of 2012 Sep 23 05:16:06 (UT). The fluxes are as measured at the location of the afterglow, whereas the AB magnitudes are corrected for Galactic foreground extinction (from Schlafly & Finkbeiner 2011), and in cases of no significant detection are reported as 2σ upper limits.

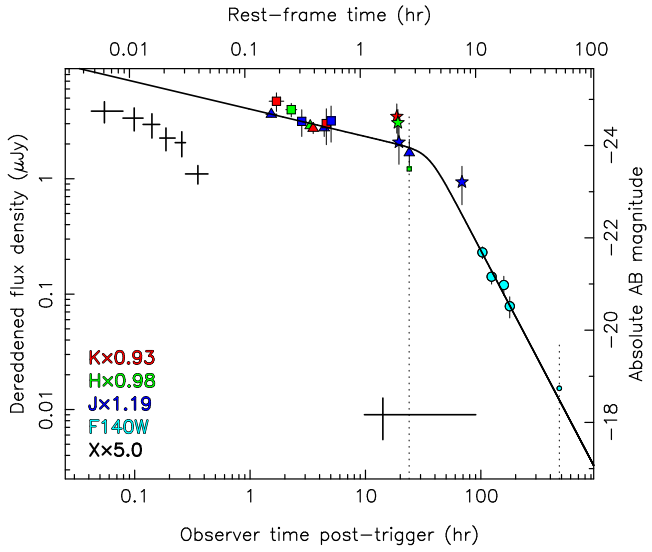

Figure 2. Infrared and X-ray light curves of GRB 120923A. The NIR measurements have been corrected for extinction by Milky Way foreground absorption using $A_B = 0.40$ (Schlafly & Finkbeiner 2011), and scaled to overlap as indicated in the key. Each telescope is plotted as a different symbol (square - UKIRT; triangle - Gemini-North; star - VLT; circle - *HST*); small symbols indicate no significant detection at 2σ. Horizontal bars represent the duration of the observation, and vertical error bars are the 1σ photometric uncertainties, except in the cases of no significant detection, where instead the line is dotted and extends to 2σ. A smoothly broken power-law model is plotted through the data: the early decay is very shallow, with $\alpha \approx -0.25$, but the break at about 35 hr leads to a steep $\alpha \approx -2$ decay (Note, an afterglow model fit to the full multiwavelength data-set is shown in Figure 11). The alternative axes showing rest-frame properties assuming a redshift of $z = 8$. The black points are XRT observations modelled at 1 keV, and the x and y bars representing the durations of the bins and the photometric uncertainties, respectively. The decline rate of the X-ray light curve before 10 h is considerably steeper than that of the NIR light curve over the same period.

are not reported since they are shallower than the corresponding VLT observations obtained at almost the same time), and present the resulting light curves in Figure 2. Constraints on the photometric redshift are outlined in Section 3.1.

2.3. *Ground-based spectroscopy*

Our first spectrum of the afterglow was obtained with the VLT/X-shooter spectrograph (Vernet et al. 2011) together with the K-band blocking filter, beginning 0.78 days post-burst (Table 3). The slit width was fixed at $0\farcs9$, which is reasonably matched to the $\approx 1\farcs0 - 1\farcs1$ seeing. The target was acquired by offsetting from a nearby bright star.

We nodded the target between two positions (A and B, separated by $5''$) on the slit and took exposures in an 'ABBA' sequence, as is usual for X-shooter. This was repeated at two different position angles of the slit, specifically 157.6° and -161.8° (defined from N through E), which maintained an approximately parallactic position. The data were reduced using the X-shooter pipeline (Goldoni 2011). The spectra were first rectified and re-sampled to produce linear spectra on a uniform 0.6 Å pix^{-1} wavelength scale. Preliminary sky subtraction was done by differencing neighbouring frames. No continuum trace was visible at this stage. We refined the sky subtraction by masking out the brightest sky lines, and subtracting any residual sky signal channel by channel. Atmospheric throughput variations were calibrated by reference to observations of two telluric standard stars (Hip094250, Hip094986) obtained close in time to the science data. Channels with the highest telluric absorption ($> 50\%$), bad pixels, and other image artefacts were all masked out. Finally, we co-added all the frames weighted by their respective signal-to-noise ratios, and optimally binned the data in wavelength to produce wide, 30 Å, channels. This revealed a weak but clear trace at the expected position on the slit in the NIR arm (which covers wavelength range $\sim 1.02 - 1.8\,\mu$m). We normalized the absolute flux scale of the spectrum to match the J-band photometry at the same epoch. No signal was detected in either the UVB ($\sim 0.35-0.56\,\mu$m) or VIS ($\sim 0.56 - 1.02\,\mu$m) arms. The spectroscopic redshift we deduce is presented in Section 3.2.

2.4. *Hubble Space Telescope observations*

We triggered our cycle 19 *Hubble Space Telescope* (*HST*) program to acquire slit-less grism spectroscopy of the afterglow with the Wide-Field Camera 3-IR (WFC3-IR), in addition to further imaging in the NIR using the F140W filter (approximately a wide JH-band). We photometered the afterglow in the F140W images using a $\approx 0\farcs32$ radius aperture, adopting the standard *HST* zero-point calibration and aperture correction for this filter. This sequence of observations, beginning at 4.3 days post-burst, revealed a marked steepening of the light curve compared to the previous J-band decline rate of $\alpha_J \approx -0.25$ ($F_\nu \propto t^\alpha$) between ~ 2 hr and ~ 1 days (see Figure 2 and Section 4.2). As a consequence of this unexpectedly rapid fading of the afterglow, combined with challenges due to overlapping traces from faint sources in the crowded field, no usable grism spec-

Table 3. GRB 120923A: Log of spectroscopic observations

$\Delta t_{\rm start}$(hr)	$\Delta t_{\rm end}$ (hr)	Telescope/Camera	Spectral element	Exp. (min)
18.69	21.69	VLT/X-shooter	-	160
102.3	104.6	*HST*/WFC3-IR	G141	80
158.1	160.4	*HST*/WFC3-IR	G141	80
172.5	173.2	*HST*/WFC3-IR	G141	40
183.7	184.4	*HST*/WFC3-IR	G141	40

NOTE— The start and end time of each observation is relative to the BAT trigger time of 2012 Sep 23 05:16:06 (UT).

trum could be extracted. We report our F140W photometry in Table 2 and do not consider the grism data further in our analysis.

2.5. *Radio observations*

We observed GRB 120923A with the Combined Array for Research in Millimeter Astronomy (CARMA) beginning on 2012 Sep 23.99 UT (0.77 days after the burst) at a mean frequency of 85 GHz. We found no significant millimetre emission at the position of the NIR counterpart or within the enhanced *Swift*/XRT error circle to a 3σ limit of 0.39 mJy.

We observed the afterglow in the C (4–7 GHz; mean frequency 6.05 GHz) and K (18–25 GHz; mean frequency of 21.8 GHz) radio bands using the Karl G. Jansky Very Large Array (VLA) starting 0.82 days after the burst. Depending on the start time of the observations, we used either 3C286 or 3C48 as the flux and bandpass calibrator. We used J1950+0807 as gain calibrator and carried out data reduction using the Common Astronomy Software Applications package (`CASA`[4]).

A possible weak source was seen at 7.9 days in the C band with flux density $25 \pm 8\,\mu$Jy. We followed up this putative radio afterglow through a VLA Director's Discretionary Time proposal (12B-387, PI: Zauderer) over a period of 44 days (Figure 3). The C band observations at 11.8 days also show a marginally significant peak in the flux density map, but the position is offset from that of the previous epoch by $\approx 2\sigma$. No significant source is detected in the subsequent C band epochs nor in the K band data within the Gemini-North error circle. Detailed examination and stacking analyses of the images suggests that the two possible detections in the C band are likely due to noise. We therefore consider the VLA observations to yield a non-detection of the radio afterglow, and report the upper limits and formal photometric point source fits derived from the maps and stacks in Table 4.

[4] https://casa.nrao.edu/

3. REDSHIFT DETERMINATION

3.1. *Photometric redshift constraints*

We first investigate the redshift constraints from the optical-NIR spectral energy distribution (SED) of the afterglow, using techniques similar to those described in Laskar et al. (2014). For uniformity, we selected observations from a single telescope for this analysis, specifically the Gemini-North/GMOS riz measurements and the Gemini-North/NIRI $YJHK$ measurements obtained within 5 hr post-burst. We corrected these data for Galactic extinction, using $A_{\rm V,gal} = 0.4$ mag (Schlafly & Finkbeiner 2011), and the Milky Way extinction model of Pei (1992). The photometry was interpolated to a common time corresponding to the NIRI H-band observation, using a power law fit to the J-band light curve between 0.06 days and 1.0 days, the latter yielding $\alpha_{\rm J} = -0.252 \pm 0.022$. We added the interpolation uncertainty in quadrature with the photometric uncertainty to determine the total uncertainty at each point on the SED.

We assumed the intrinsic spectrum of the afterglow is a power law, $F_\nu \propto \nu^\beta$, and used the sight-line-averaged model for the optical depth of the IGM from Madau (1995), accounting for Lyα absorption by neutral hydrogen and photoelectric absorption by intervening systems. We also included Lyα absorption by the host galaxy interstellar medium (ISM), for which we assumed a column density of $\log(N_{\rm H}/{\rm cm}^{-2}) = 21.1$, the mean value for GRBs at $z \sim$ 2–3 (Fynbo et al. 2009), although within the errors the photometric redshift is insensitive to the exact value chosen. The free parameters in our model are the redshift of the GRB, the extinction along the line of sight within the host galaxy (A_V), and the spectral index (β) of the afterglow SED. The SMC dust extinction law of Pei (1992) was assumed to model the extinction in the host galaxy, $A_{\rm V}$(this is likely

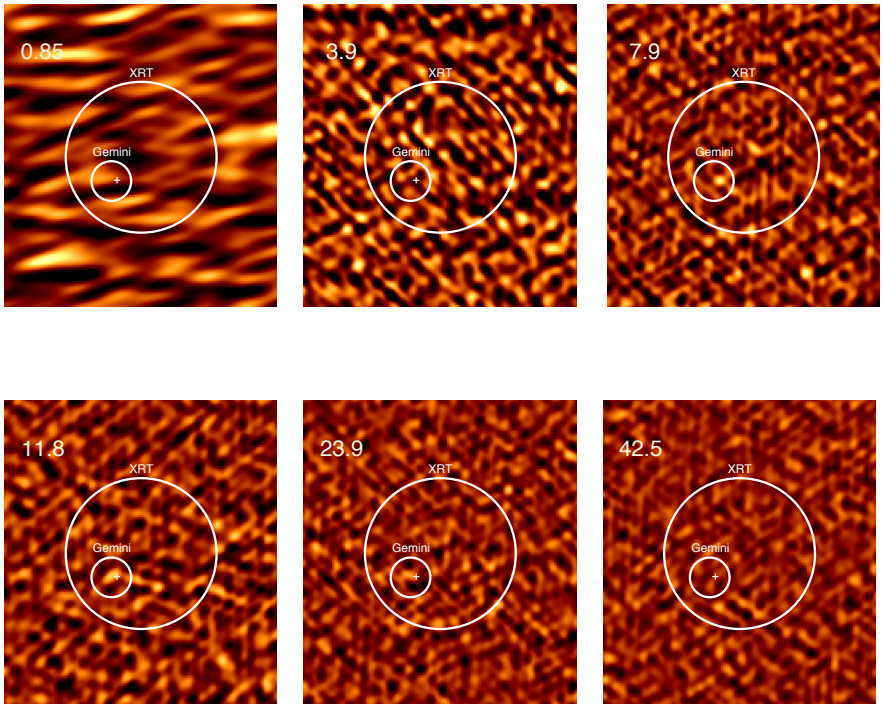

Figure 3. 6.05 GHz C band VLA images of the field of GRB 120923A, together with the XRT and Gemini-North error circles. The cross marks the location of the $\approx 3\sigma$ possible source in the observation at 7.9 days. The position of the peak at 11.8 d is offset from that at 7.9 days, suggesting that this is not a real radio source. The last image is the stack of observations taken at 40.8 days and 43.8 days. We conclude that no radio afterglow was detected for this GRB.

Table 4. Millimeter and Radio Observations of GRB 120923A

Epoch	$t - t_0$ (days)	Observatory	Band	Frequency (GHz)	Integration Time (min)	3σ Upper Limit (μJy)
1	0.77	CARMA	3 mm	85.0	...	< 390
1	0.824	VLA	K	21.8	17.7	< 69.1
1	0.853	VLA	C	6.05	19.9	< 29.7
2	3.90	VLA	K	21.8	18.1	< 64.4
2	3.91	VLA	C	6.05	17.4	< 31.0
3	7.91	VLA	C	6.05	27.8	< 22.5
4	11.8	VLA	C	6.05	35.5	< 20.1
5	23.9	VLA	C	6.05	37.9	< 17.1
6	40.8	VLA	C	6.05	36.3	< 18.4
7	43.8	VLA	C	6.05	49.5	< 15.8
3&4*	10.1†	VLA	C	6.05	63.4	< 15.5
6&7*	42.5†	VLA	C	6.05	85.8	< 14.8

NOTE—* Stacks. †The reported value of $t - t_0$ for stacks is weighted by the integration time of the individual observations used in the stack.

to be appropriate for the expected low metallicity host galaxy, and has also often found to be a good approximation to the extinction laws in the majority of lower redshift GRB hosts e.g., Schady et al. 2012; Perley et al. 2013). We took a flat prior for the redshift and the extinction, and employed the distribution of extinction-corrected optical-NIR spectral slopes, β_o from Greiner et al. (2011) as a prior on β.

Fitting was performed using a Markov Chain Monte Carlo (MCMC) algorithm to explore the parameter space, integrating the model over the filter bandpasses, and computing the likelihood of the model by comparing the resulting fluxes with the observed values using a `Python` implementation of the ensemble MCMC sampler `emcee` (Foreman-Mackey et al. 2013). The resulting 68% confidence intervals about the median values for the fitted parameters are $z = 8.1 \pm 0.4$, $\beta = -0.17^{+0.34}_{-0.25}$, and $A_V = 0.07^{+0.09}_{-0.05}$ mag, where the large errors on β reflect the limited lever arm obtained from the three JHK detections. The highest-likelihood model is $z \approx 7.79$, $\beta \approx -0.39$, and $A_V \lesssim 0.1$ mag, and this is shown, along with a model with the median parameters, in Figure 4. The full posterior density function for the redshift is shown in Figure 5, and allows us to rule out a redshift of $z \lesssim 7.3$ at 99.7% confidence.

3.2. *Spectroscopic redshift*

The X-shooter spectrum (Figure 6) exhibits significant flux redward of 1.2 μm (below 2.5×10^{14} Hz), with a spectral slope of $\beta = -0.6 \pm 0.5$, and a steep cut-off blueward of $\approx 1.1\,\mu$m. We model the spectrum as a power law with index β, and interpret the break as due to Lyα absorption by neutral hydrogen in the host galaxy followed by a Gunn-Peterson trough blueward of the host absorption. We proceed with the remainder of the analysis as for the photometric redshift, assuming a flat prior for the redshift and the extinction, and again using the distribution of β_o from Greiner et al. (2011) as a prior on β. We also fix the neutral hydrogen column density of the host galaxy to $\log(N_{\rm HI,host}/{\rm cm}^{-2}) = 21.1$ (Section 3.1); a significantly higher column than this is unlikely given the evidence for low extinction and the suggestion of a trend toward somewhat lower columns seen in GRBs at $z \gtrsim 6$ (Chornock et al. 2014), whilst assuming a lower value for $N_{\rm HI,host}$ does not change the derived redshift within the errors.

However, instead of integrating over filter bandpasses, we fitted the model directly to the observed X-shooter NIR spectrum. We find $z = 7.84^{+0.06}_{-0.12}$, $\beta = -0.54 \pm 0.40$, and $A_V = 0.17^{+0.09}_{-0.12}$, where the uncertainties reflect 68% credible intervals about the median. We plot our best-fit model in Figure 6. The best fit parameters are $z \approx 7.8$, $\beta \approx -0.54$, and $A_V \approx 0.17$, all consistent with the median values, and with the photometric redshift of $z = 8.1 \pm 0.4$ (Section 3.1).

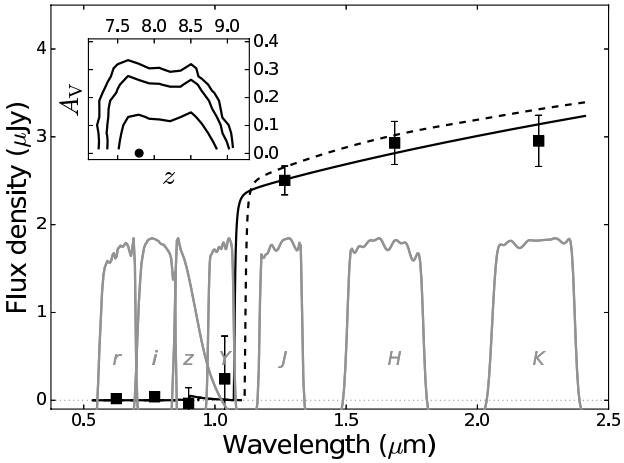

Figure 4. The optical-to-NIR spectral energy distribution of GRB 120923A at 0.14 days. The JHK photometry has been extrapolated from the nearest Gemini-North detections using a fit to the J-band light curve between 1.4 h and 24 h ($\alpha_J = -0.252 \pm 0.022$). The $rizY$ points are from forced photometry on Gemini-North images in the same time interval, also interpolated using the J-band light curve. All photometry (including the z-band formal negative flux measurement) has been multiplied by a factor > 1 to correct for Galactic extinction ($A_B = 0.4$; Schlafly & Finkbeiner 2011). The data points have been placed at the centroid of the filter bandpasses for clarity. The lines are models for the afterglow SED, including IGM and ISM absorption using the highest-likelihood model (solid) and the median values of the parameter distributions (dashed). We show the 1σ, 2σ, and 3σ correlation contours between extinction (A_V) and redshift (z) in the inset, where the black dot indicates the highest-likelihood model.

4. BURST PROPERTIES AND COMPARISON TO THE LONG-GRB POPULATION

4.1. *High energy behaviour*

At $z \approx 7.8$, the BAT peak flux corresponds to a luminosity, $L_{\rm iso} \approx 3.2 \times 10^{52}\,{\rm erg\,s^{-1}}$. In Figure 7 we show the peak luminosity for all the *Swift* GRBs with measured redshifts to March 2015. The low energy cut-off imposed by the BAT selection function indicates that only GRBs at the bright end of the luminosity function can be detected at $z > 6$, despite *Swift* utilizing a variety of algorithms to try to recover even time-dilated bursts (e.g, Lien et al. 2014). It is clear that GRB 120923A was close to this detection limit, and the intrinsically faintest event found at $z > 6.5$ to-date.

In Figure 8, we compare the X-ray light curve of GRB 120923A to those of a large sample of *Swift* bursts

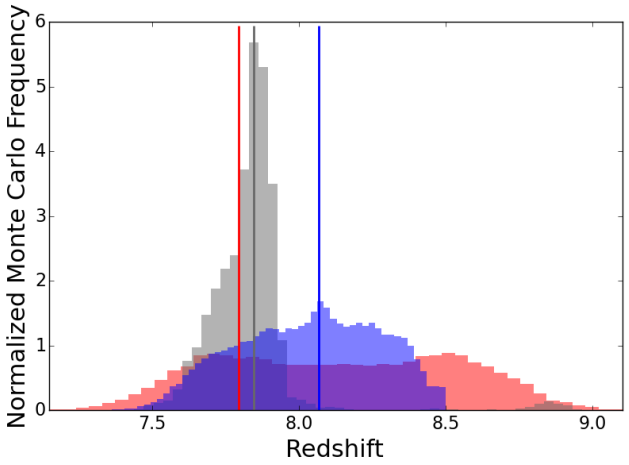

Figure 5. Posterior density function for the redshift of GRB 120923A from fitting the photometric SED (red, Figure 4 and Section 3.1), from fitting the NIR spectrum (grey, Figure 6 and Section 3.2), and from fitting all the available X-ray to radio afterglow data (but not the X-Shooter spectrum) with a physical multi-wavelength model (blue; Section 5.3). The vertical lines indicate the redshifts of the respective best-fit models.

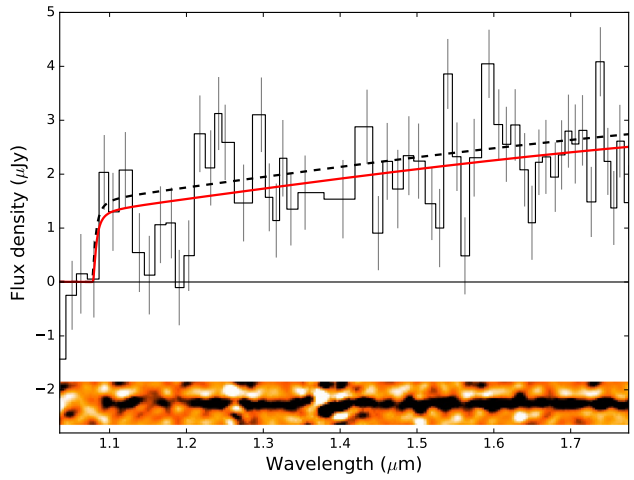

Figure 6. VLT/X-shooter spectrum of the GRB 120923A afterglow. The 1D data have been adaptively binned so that the noise in each bin is approximately the same. The 2D spectrum has been re-binned and smoothed to enhance the trace of the afterglow. The lines are models for the afterglow spectrum, including IGM and ISM absorption using the highest-likelihood model (red, solid) and the median values of the parameter distributions (dashed).

(Evans et al. 2009). We find that GRB 120923A was amongst the faintest long-duration GRB afterglows seen by XRT. Another view of these data is shown in Figure 9, in which each burst has been shifted to show how it would have appeared if it were at $z = 8$ (we also

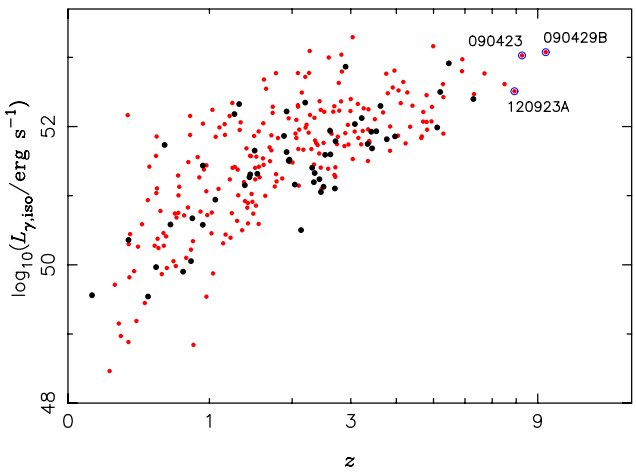

Figure 7. The 1 s peak fluxes in the observed 15–150 keV band (Sakamoto et al. 2011; Lien et al. 2016) converted to rest-frame isotropic-equivalent luminosities for all *Swift* bursts with redshifts to March 2015. The bursts from the TOUGH sample (Hjorth et al. 2012; Jakobsson et al. 2012; Krühler et al. 2012) are black points, and the three highest redshift bursts are individually labelled. The effective selection function imposes the lower envelope to this distribution, although note that in practice the sensitivity of BAT depends on the instantaneous background count rate, the location of the burst within its field of view and the structure of the light curve.

show the corresponding rest-frame axes). In this case we restrict the low redshift sample to the events included in The Optically-Unbiased GRB Host survey (TOUGH; Hjorth et al. 2012). The high redshift completeness of that sample minimises any optical selection biases. This shows that GRB 120923A was rather typical in terms of its intrinsic X-ray behaviour.

4.2. *Infrared behaviour*

We present the GRB 120923A composite NIR light curve formed by the JHK and F140W photometry in Figure 2, scaling the JHK bands by small factors to match the F140W band. A fit to this overall light curve of a broken power-law model yields a shallow initial slope, $\alpha_1 \approx -0.25$, breaking at ≈ 35 hours to a steep decay with $\alpha_2 \approx -1.9$ ($\chi^2/{\rm dof} = 12.1/13$). We compare the light curve to other high-redshift GRBs in Figure 10. The afterglow of GRB 120923A is comparatively faint, and could easily have escaped detection in other circumstances; i.e. we were lucky in being able to observe the afterglow with an 8-m telescope in excellent seeing within 2 hours, and to continue observations for several hours before the source set. Since the peak flux density of the afterglow SED is directly proportional to

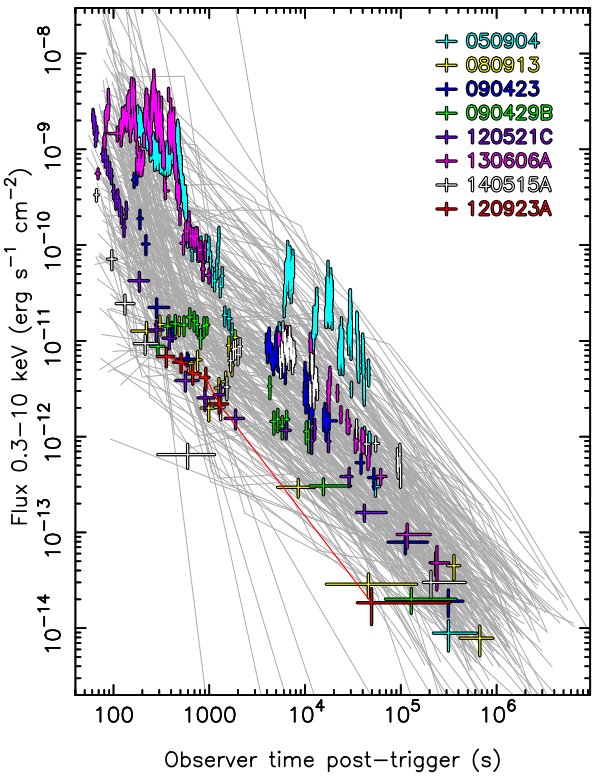

Figure 8. Multiply-broken power-law fits to the light curves in the 0.3–10 keV X-ray band for a large sample of *Swift* long duration GRBs (Evans et al. 2009) in grey, and high-z GRBs (GRB 130606A at $z = 5.9$, GRB 120521C at $z \approx 6.0$, GRB 140515A at $z = 6.3$, GRB 050904 at $z = 6.3$, GRB 080913 at $z = 6.7$, GRB 090423 at $z = 8.2$, and 090429B at $z \approx 9.4$) in colour. Data for GRB 120923A are shown in red points, illustrating that it was amongst the faintest afterglows seen by *Swift*, and factors of several fainter at late times, compared to other $z \gtrsim 6$ events.

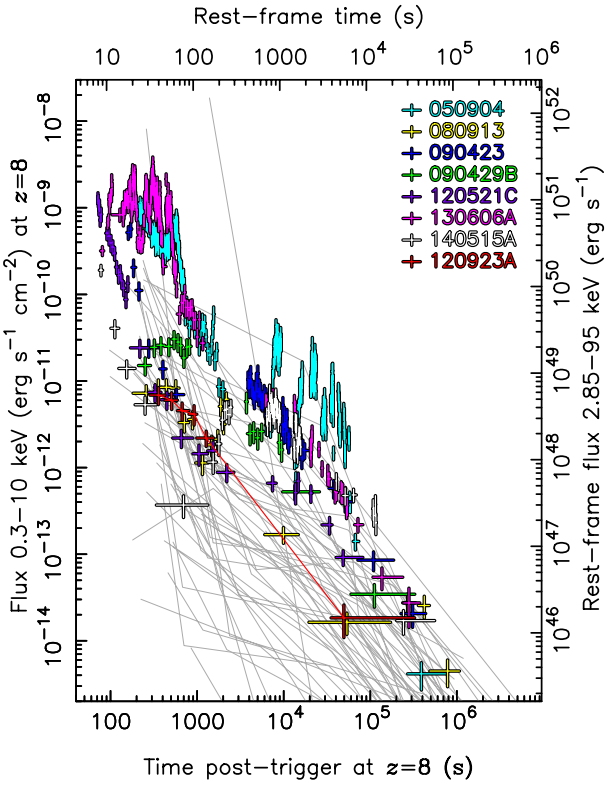

Figure 9. Multiply-broken power-law fits to the X-ray light curves of the TOUGH sample of GRBs (Hjorth et al. 2012), in grey, together with a selection of very high-z bursts (see caption to Fig. 8), redshifted to show how they would appear at $z = 8$ observed by *Swift*. In terms of its intrinsic X-ray light curve (see alternative axes), GRB 120923A is more typical of the TOUGH sample, whilst GRB 090423, and particularly GRB 050904 would have been amongst the brightest in the rest frame.

the blastwave kinetic energy (Granot & Sari 2002), the relative faintness may result at least in part from a comparatively low value of $E_{\rm K}$. We investigate this further via multi-wavelength modelling in Section 5.

It is interesting to note that the SED of this afterglow is comparatively blue ($\beta = -0.17^{+0.34}_{-0.25}$ at ≈ 0.14 d; Figure 4 and Section 3.1), consistent with little line-of-sight dust extinction in the host, as has generally been found for other afterglows of the high-z GRBs (Zafar et al. 2011; Laskar et al. 2014). This may reflect the limited time to build up dust, particularly in the small galaxies that are likely dominating the total star formation budget at $z > 6$ (although see Watson et al. 2015, for an example of substantial dust in a galaxy at $z \approx 7.5$). Of course, there is also an observational bias against discovering dusty afterglows at high redshift. We consider the quantitative constraints on dust extinction to GRB 120923A in Section 5.3.

5. MULTI-WAVELENGTH MODELLING

5.1. *Synchrotron Model*

We now interpret the multi-wavelength observations of GRB 120923A in the context of the standard synchrotron model, in which the afterglow radiation arises from the blastwave shock set up by the expanding rel-

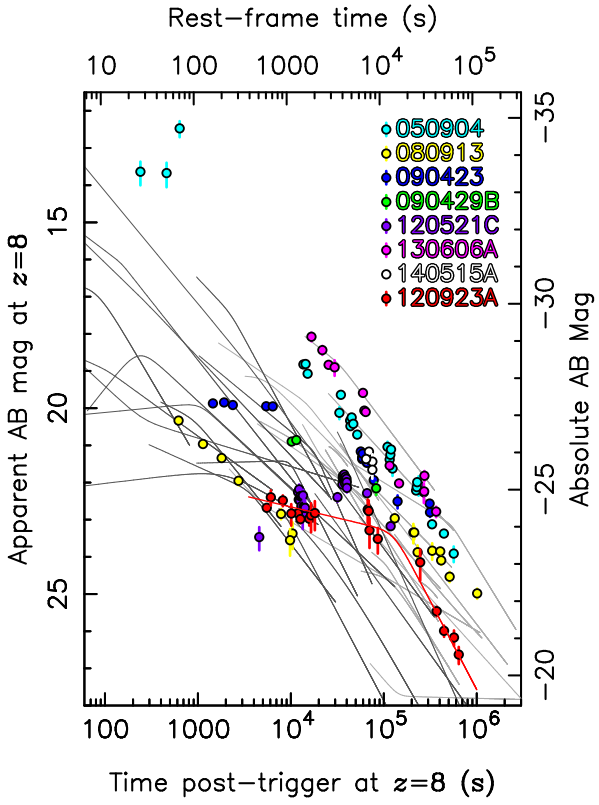

Figure 10. Infrared light curves of high redshift GRBs 120923A, 130606A (Hartoog et al. 2015), 120521C (Laskar et al. 2014), 050904 (Boër et al. 2006; Haislip et al. 2006), 080913 (Greiner et al. 2009), 090423 (Tanvir et al. 2009) and 090429B (Cucchiara et al. 2011) as they would appear at redshift $z = 8$ and also (alternative axes) rest-frame time and absolute magnitude. In grey are the broken power-law fits to light curves of a sample of low redshift afterglows from Kann et al. (2010), also transformed to the same redshift.

ativistic GRB ejecta interacting with their circumburst environment. This model assumes an idealised jet and ambient medium, but is appropriate given our limited sampling of the evolving SED. The resulting radiation is expected to exhibit characteristic power law spectral segments connected at 'break frequencies', namely the synchrotron cooling frequency (ν_c), the characteristic synchrotron frequency (ν_m), and the self-absorption frequency (ν_a). The location of these frequencies depend on the physical parameters: the isotropic-equivalent kinetic energy ($E_{K,iso}$), the circumburst density (n_0, or the normalised mass-loss rate in a wind-like environment, A_*), the fraction of the blastwave energy imparted to non-thermal electrons (ϵ_e), and the fraction converted into post-shock magnetic energy density (ϵ_B).

The different possible orderings of the break frequencies (e.g., $\nu_m < \nu_c$: 'slow cooling', and $\nu_c < \nu_m$: 'fast cooling') then give rise to five possible afterglow SED shapes (Granot & Sari 2002). As the radius and Lorentz factor of the blastwave change with time, these break frequencies evolve and the afterglow SED may transition between these different spectral shapes. To preserve smooth light curves when break frequencies cross, we use the weighting schemes described in Laskar et al. (2014) to compute the afterglow SED as a function of time. As in Section 3.1, we adopt the SMC extinction curve (Pei 1992) to model the extinction in the host galaxy, A_V, and include the possibility of an achromatic 'jet-break' in the afterglow light curves due to spreading and edge-effects expected for a collimated outflow. To efficiently sample the available parameter space, we carry out an MCMC analysis using `emcee`. The details of our modelling scheme and MCMC implementation are described in Laskar et al. (2014).

5.2. *Basic Considerations*

The lack of any flattening in the late-time NIR light curve (Fig. 10) indicates that any host contamination of the afterglow photometry is small, and we assume it to be negligible in what follows. The J-band light curve declines as $\alpha_J = -0.23 \pm 0.04$ between 0.06 days and 0.2 days. In the synchrotron model, such a shallow decline in the NIR is only possible if $\nu_c \lesssim \nu_{NIR} < \nu_m$, where the lightcurves decline as $t^{-1/4}$ regardless of the density profile of the circumburst environment. This suggests that the afterglow radiation is in the fast cooling regime, and that the NIR bands are on segment F of Granot & Sari (2002). In this scenario, we would expect the light curve to steepen to $\alpha = (2 - 3p)/4$ when $\nu_m \propto t^{-3/2}$ passes through the NIR band, where p is the power-law index of the electron energy distribution. Alternatively, in the particular case of a wind environment, $\nu_c \propto t^{1/2}$ may pass through the NIR band first, and the NIR decay rate would steepen to $\alpha = -2/3$.

The steepness of the late decay ($\alpha_J \approx -1.8 \pm 0.3$ between 4.3 days and 20 days), and marked change from the early behaviour, provides evidence that a jet break occurred at $\lesssim 4.3$ days, and also suggests the passage of ν_m through the NIR band between 0.2 and 4.3 days, and

indicates a uniform (ISM-like) environment. If we take the power law within this window, $\alpha_{\rm J} = -1.2 \pm 0.2$, as indicative of the slope after $\nu_{\rm m}$ passage, but before the jet break, then using $\alpha_{\rm J} = (2-3p)/4$ yields $p = 2.3 \pm 0.3$.

The XRT PC-mode light curve is well-fit with a broken power law, with an initial flat segment, $\alpha_{\rm X,1} = 0.0 \pm 0.2$, breaking into[5] $\alpha_{\rm X,2} = -1.32 \pm 0.05$ at $t_{\rm b} = (6.3 \pm 1.2) \times 10^{-3}$ days. The initial flat portion of the X-ray light curve may be due to the X-rays being on the same segment (F) of the synchrotron SED as the NIR data. In this case, the X-ray decline rate is also expected to be $t^{-1/4}$. The break in the X-ray light curve would then correspond to the passage of $\nu_{\rm m}$ through the X-ray band. Since the X-ray band spans an order of magnitude in energy, while $\nu_{\rm m}$ evolves as $t^{-3/2}$, we would expect the break to be smoothed out over a factor of $\approx 10^{-2/3} \approx 5$ in time. If we assumed $\nu_{\rm m} \approx \nu_{\rm J} \approx 2.2 \times 10^{14}$ Hz at ≈ 0.2 days, we would expect $\nu_{\rm m} \approx 1$ keV at $\approx 2 \times 10^{-3}$ days. This is consistent with the observed steepening in the X-ray lightcurve at $\approx 6 \times 10^{-3}$ days. In this model, the post-break decline rate of $\alpha_{\rm X} = -1.32 \pm 0.05$ yields $p = 2.43 \pm 0.07$. The different decline rates in the X-ray and NIR bands between 0.06 days and 0.2 days suggests that these bands are on different segments of the afterglow synchrotron spectrum, consistent with the spectral ordering, $\nu_{\rm c} \lesssim \nu_{\rm NIR} < \nu_{\rm m} < \nu_{\rm X}$ during this period.

The spectral index in segment F is expected to be $\beta = -0.5$, independent of p. When the X-rays are on this segment, we would expect $\Gamma_{\rm X} = 1 - \beta_{\rm X} = 1.5$, which is consistent with the value of $\Gamma_{\rm X} = 1.61 \pm 0.14$ derived in Section 2.1. We would also expect spectral evolution from $\Gamma_{\rm X} = 1.5$ to $\Gamma_{\rm X} = 1 + p/2$ after $\nu_{\rm m}$ crosses the X-ray band. Unfortunately, paucity of data following the orbital gap in the X-ray light curve precludes confirmation of this behaviour.

Interpolating the X-ray lightcurve using the best fit broken power law model, we find a flux density of $(3.5 \pm 0.4) \times 10^{-2}$ μJy at the time of the Gemini/NIRI J-band observation at 0.064 days. The spectral index between the NIR and X-ray band is then $\beta_{\rm NIR-X} \approx -0.65 \pm 0.01$. This is significantly different from -0.5, suggesting that at least one spectral break frequency lies between the NIR and X-ray band. Assuming a spectral slope of $\beta = -0.5$ and $\beta = -p/2 = -1.22$ below and above this break, respectively, and using the measured J-band flux density and extrapolated X-ray flux density, we can locate the break to be at $\approx 5.9 \times 10^{16}$ Hz at this epoch. However, extrapolating $\nu_{\rm m} \propto t^{-3/2}$ from $\approx 2.2 \times 10^{14}$ Hz at ≈ 0.2 days to 0.064 days yields $\nu_{\rm m} \approx 1.2 \times 10^{15}$ Hz, which is more than an order of magnitude lower. Here we have neglected the possibility of dust extinction in the host galaxy. A small amount of extinction would lead us to overestimate $\beta_{\rm NIR-X}$ and hence overestimate $\nu_{\rm m}$, and so in principle alleviate this discrepancy. However, we estimate that requiring $\beta_{\rm NIR-X} \approx \beta_{\rm X}$ would necessitate $A_{\rm V} \gtrsim 0.2$, which is disfavored from our analysis of the NIR photometry in Section 3.1. We return to the question of host extinction in Section 5.3.

[5] The smoothness (y in Laskar et al. 2014; equivalent to s in Granot & Sari 2002) of the break is poorly constrained, and we fix it to $y = 3$.

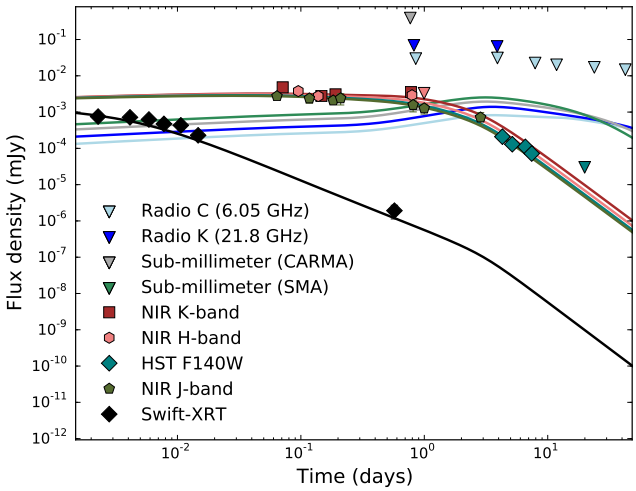

Figure 11. X-ray, NIR, and radio light curves of GRB 120923A, with the best-fit model (solid lines) fitted simultaneously to all the available multi-wavelength data.

In the synchrotron model, we can use the observed X-ray flux density at 1 keV at a time that is dominated by afterglow radiation to estimate the burst kinetic energy (e.g. Granot et al. 2006). This requires the X-ray band to be located above the peak and cooling frequencies. Since $\nu_{\rm c}, \nu_{\rm m} < \nu_{\rm X}$ after the break in the X-ray light curve, this condition is satisfied. We use the last point preceding the *Swift* orbital gap with $f_{\rm X} \approx 0.22$ μJy at ≈ 0.36 hr, together with fiducial values of $p = 2.2$ (e.g., Curran et al. 2010) and $\epsilon_{\rm e} = \epsilon_B = 1/3$ to estimate $E_{\rm K,iso} \approx 3 \times 10^{51}$ erg. We verify this result in the next section.

To summarise, the X-ray light curve, X-ray spectrum, and NIR J-band light curve suggest that the observed synchrotron radiation from the blastwave shock is in the fast cooling regime with $\nu_{\rm c} \lesssim \nu_{\rm NIR} < \nu_{\rm m} < \nu_{\rm X}$ at ≈ 0.2 days; $\nu_{\rm m}$ passes through the X-ray band at about a few $\times 10^{-3}$ days, and through the J-band between ≈ 0.2 days and 4.3 days, while the steep decline in the *HST* F140W data indicates a jet break before ≈ 4.3 days.

5.3. *Multi-wavelength Model for GRB 120923A*

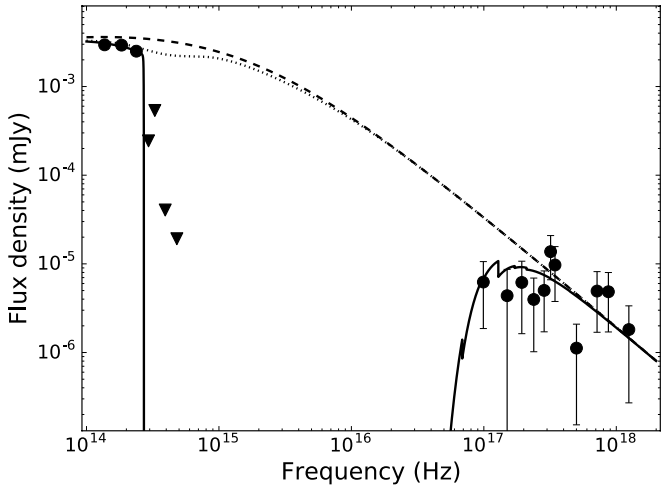

Figure 12. NIR to X-ray SED of the GRB 120923A afterglow at 0.14 days together with the best-fit model (solid). The NIR observations are the same points used in Figure 4 and have been corrected for Galactic extinction. The X-ray SED is computed from PC-mode data after 1.1×10^{-2} days and interpolated to 0.14 days using the X-ray light curve decline rate of $\alpha_{\rm X,2} \approx -1.32$ (Section 5.2). The intrinsic afterglow synchrotron SED (without IGM absorption or host extinction) is shown as the dashed black curve, while the dotted curve is the intrinsic SED with $A_{\rm V} = 0.06$ mag of extinction in the host galaxy. Although a small amount of extinction is present in the best fit model, our MCMC analysis indicates that overall evidence for extinction in the host galaxy along the line of sight is marginal.

We now describe the full multi-wavelength modelling of all available afterglow data for GRB 120923A using the techniques presented in Laskar et al. (2014), which include accommodating upper limits. We adopted weak, flat priors based on plausible ranges: $2.01 < p < 3.45$, $\epsilon_{\rm e}, \epsilon_B < 1/3$, $-10 < \log(n_0/{\rm cm}^{-3}) < 10$, $-4 < \log(E_{\rm K,iso}/10^{52}\,{\rm erg}) < 2.7$, $A_{\rm B} < 20$ mag, and $-5 < \log(t_{\rm jet}/{\rm d}) < 5$. For the sake of generality, we did not fix the redshift, but based on our analysis of the NIR spectral energy distribution (Section 3.2) restricted the redshift range to $7.0 < z < 8.5$.

We find that an ISM-like model with a jet break adequately explains the full set of afterglow observations. Our highest likelihood model (Figure 11) has the parameters $p \approx 2.5$, $z \approx 8.1$, $\epsilon_{\rm e} \approx 0.33$, $\epsilon_B \approx 0.32$, $n_0 \approx 4.0 \times 10^{-2}\,{\rm cm}^{-3}$, and $E_{\rm K,iso} \approx 2.9 \times 10^{51}$ erg, with a jet break at $t_{\rm jet} \approx 3.0$ days ($\chi^2/{\rm dof} = 1.1$). We note that the derived value of $E_{\rm K,iso}$ confirms the estimate made using the X-ray data (Section 5.2). An implication of this is a very high value for the radiative efficiency $\eta = E_{\gamma,\rm iso}/(E_{\gamma,\rm iso} + E_{\rm K,iso}) \approx 0.92$. Such high values for η have also been inferred for the prompt emission of some other GRBs (e.g. Zhang et al. 2007), although they remain a challenge to explain theoretically.

Thus the redshift derived by this approach is completely consistent with the photometric redshift found in Section 3.1. This model requires a small amount of extinction in the host galaxy, $A_{\rm V} \approx 0.06$ mag (Figure 12). Using the relation,

$$\theta_{\rm jet} = 0.1 \left(\frac{n_0}{E_{\rm K,iso}/10^{52}}\right)^{1/8} \left(\frac{t_{\rm jet}/(1+z)}{6.2\,{\rm hr}}\right)^{3/8} \quad (1)$$

for the jet opening angle (Sari et al. 1999) we find $\theta_{\rm jet} \approx 4.9$ degrees and beaming-corrected kinetic energy, $E_{\rm K} \approx 1.1 \times 10^{49}$ erg.

The break frequencies are located at $\nu_{\rm ac} \approx 3 \times 10^7$ Hz, $\nu_{\rm sa} \approx 7 \times 10^7$ Hz, $\nu_{\rm c} \approx 6 \times 10^{14}$ Hz, and $\nu_{\rm m} \approx 3 \times 10^{15}$ Hz at 0.1 days and the peak flux density is $\approx 13\,\mu$Jy at $\nu_{\rm c}$ for the highest-likelihood model. In this model, $\nu_{\rm m}$ passes through 1 keV at $\approx 5 \times 10^{-3}$ days, which is precisely the time of the observed break in the X-ray light curve, $t_{\rm b} = (6.3 \pm 1.2) \times 10^{-3}$ days (Section 5.2). The shallow-to-steep transition in the X-ray light curve is therefore consistent with the passage of $\nu_{\rm m}$.

We note that the spectrum peaks at $\nu_{\rm c}$ in the fast cooling regime, and the proximity of the cooling break to the NIR J-band at ≈ 0.1 days results in a spectrum near the J-band that is flatter than $\nu^{-0.5}$. This explains the lower value of $\nu_{\rm m}$ (which lies between $\nu_{\rm c}$ and $\nu_{\rm X}$) inferred from the NIR and X-ray light curves, compared with the value required in a broken power-law fit to match the NIR J-band and interpolated X-ray flux density at this time. The location of $\nu_{\rm c} \gtrsim \nu_{\rm J}$ at 0.1 d rules out the wind model, since in that case we would expect the NIR light curve to decline as $t^{-2/3}$ after ≈ 0.1 d (Section 5.2). The passage of $\nu_{\rm m}$ through the NIR J-band occurs at ≈ 0.5 days, at which point both $\nu_{\rm c}$ and $\nu_{\rm m}$ are below $\nu_{\rm J}$ and the light curve steepens to $\alpha \approx -1.4$, consistent with the limited observations at this time. Finally, the best-fit model requires a jet break at ≈ 3 days.

In broad agreement with the basic analysis presented in Section 5.2, the model afterglow SED remains in fast cooling until ≈ 0.34 days (approximately 1 hr in the rest-frame). This conclusion is driven in the fit by the apparent change in NIR spectral slope between the early data, particularly the Gemini photometry at ~ 0.14 days and the VLT epoch at ~ 0.8 days, as illustrated in Figure 13.

From our MCMC simulations, we constrain the fitting parameters to $p = 2.7^{+0.3}_{-0.2}$, $z = 8.1^{+0.2}_{-0.3}$, $\epsilon_{\rm e} = 0.31^{+0.02}_{-0.04}$, $\epsilon_B = 0.23^{+0.07}_{-0.11}$, $n_0 = (4.1^{+2.2}_{-1.4}) \times 10^{-2}\,{\rm cm}^{-3}$, $E_{\rm K,iso} = (3.2^{+0.8}_{-0.5}) \times 10^{51}$ erg, $t_{\rm jet} = 3.4^{+1.1}_{-0.5}$ days (68% credible intervals), and $A_{\rm V} \lesssim 0.08$ mag (90% confidence upper limit). Thus, although the best-fit model has a small amount of extinction (Figure 12), our MCMC results

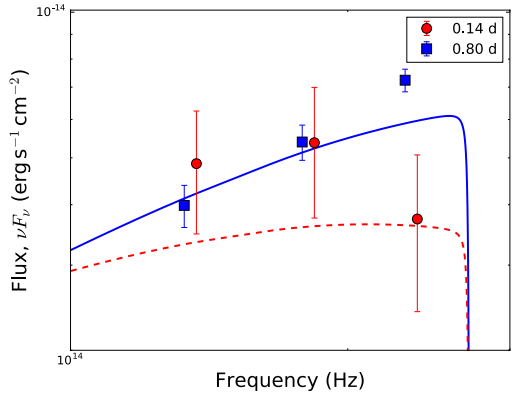

Figure 13. Spectral energy distribution (νf_ν) of the *JHK* afterglow of GRB 120923A at at 0.14 days (red circles) and 0.8 days (blue squares), together with the best fit multi-wavelength model (dashed and solid, respectively; Section 5.3). The change in the slope of the SED is evident in the data, and is ascribed in the model to the transition of $\nu_{\rm m}$ and $\nu_{\rm c}$ through the NIR bands after the transition to slow cooling at ≈ 0.34 days.

indicate that evidence for dust along the line of sight is statistically marginal.

Applying the expression for $\theta_{\rm jet}$ above to our MCMC chains with their individual values of $E_{\rm K,iso}$, n_0, z, and $t_{\rm jet}$, we find $\theta_{\rm jet} = 5.0^{+1.3}_{-0.8}$ degrees and $E_{\rm K} = (1.2^{+0.5}_{-0.2}) \times 10^{49}$ erg. Correcting $E_{\gamma,\rm iso}$ for beaming using this measurement of $\theta_{\rm jet}$, we find $E_\gamma = (1.8 \pm 0.8) \times 10^{50}$ erg. We present histograms of the marginalized posterior density for each parameter in Figure 14 and correlation contours between the physical parameters and expected relations between the parameters in the absence of constraints on one of the spectral break frequencies in Figure 15. We summarise the results of our MCMC analysis in Table 5.

Table 5. Parameters from multi-wavelength modelling of GRB 120923A

Parameter	Best-fit value	MCMC result
z	8.1	$8.1^{+0.2}_{-0.3}$
p	2.5	$2.7^{+0.3}_{-0.2}$
$\epsilon_{\rm e}$	0.33	$0.31^{+0.02}_{-0.04}$
ϵ_B	0.32	$0.23^{+0.07}_{-0.11}$
n_0(cm^{-3})	4.0×10^{-2}	$(4.1^{+2.2}_{-1.4}) \times 10^{-2}$
$E_{\rm K,iso}$ (10^{51} erg)	2.9	$3.2^{+0.8}_{-0.5}$
$t_{\rm jet}$(d)	3.0	$3.4^{+1.1}_{-0.5}$
$\theta_{\rm jet}$(degrees)	4.9	$5.0^{+1.3}_{-0.8}$
$A_{\rm V}$(mag)	0.06	$\lesssim 0.08^{\dagger}$
$E^{\ddagger}_{\gamma,\rm iso}$ (10^{52} erg)		$4.8^{+6.1}_{-1.6}$
E_γ (10^{50} erg)	1.8	$1.8 \pm 0.8^{*}$
$E_{\rm K}$ (10^{49} erg)	1.1	$1.2^{+0.5}_{-0.2}$

NOTE—† 90% confidence upper limit. The median value of the host extinction in our MCMC analysis is $A_{\rm V} = 3.8 \times 10^{-5}$ mag with a 68% credible interval $A_{\rm V} \in (0.00, 0.06)$. ‡ 1–$10^4$ keV, rest frame. * Using symmetrized uncertainties (one-half positive error minus negative error) for both $E_{\gamma,\rm iso}$ and $\theta_{\rm jet}$, followed by a Monte-Carlo calculation.

6. DISCUSSION

The photometric redshift derived from SED-fitting ($z = 8.1 \pm 0.4$) and multi-wavelength modelling ($z = 8.1^{+0.2}_{-0.3}$) agree with the redshift derived from the X-shooter spectrum ($z = 7.84^{+0.06}_{-0.12}$). As expected, the multi-wavelength modelling produces a narrower posterior density function compared to SED-fitting alone, while the spectral analysis providing the strongest constraint of the three methods. In principle, it is possible to use the posterior density function of z derived from the spectrum as a prior on the redshift for the multi-wavelength analysis. However, a perusal of the correlation contours between the redshift and the other parameters in the MCMC results of the multi-wavelength analysis suggests that the redshift is not strongly coupled to the other parameters and that, therefore, imposing such a prior is of limited utility. In confirmation, we find that selecting the multi-wavelength analysis MCMC samples within the redshift range $7.72 < z < 7.90$ (the 68% credible interval from the spectral analysis) results in identical posteriors for the other parameters as for the full distribution. The lack of a strong correlation between z and the other parameters suggests that the measurement of z is driven by a small subset of the data, essentially in a model-independent fashion.

To place our measured value of the circumburst density for GRB 120923A in context, we compute summary statistics for the circumburst density for GRBs with ISM-like environments reported and aggregated in Laskar et al. (2014) and Laskar et al. (2015). Since the density spans several orders of magnitude and therefore acts as a scale parameter, we use $\varrho \equiv \log_{10}(n_0/{\rm cm}^{-3})$ for this analysis. We find $\bar{\varrho} = -0.19$, the standard deviation, $\sigma_\varrho = 2.0$, and the median, $\hat{\varrho} = -0.17$. In comparison, we have $\varrho = -1.4 \pm 0.2$ for GRB 120923A, such that $|(\varrho - \bar{\varrho})|/\sigma_\varrho \approx 0.6$. Whereas the measured density is lower than both the mean and median reported

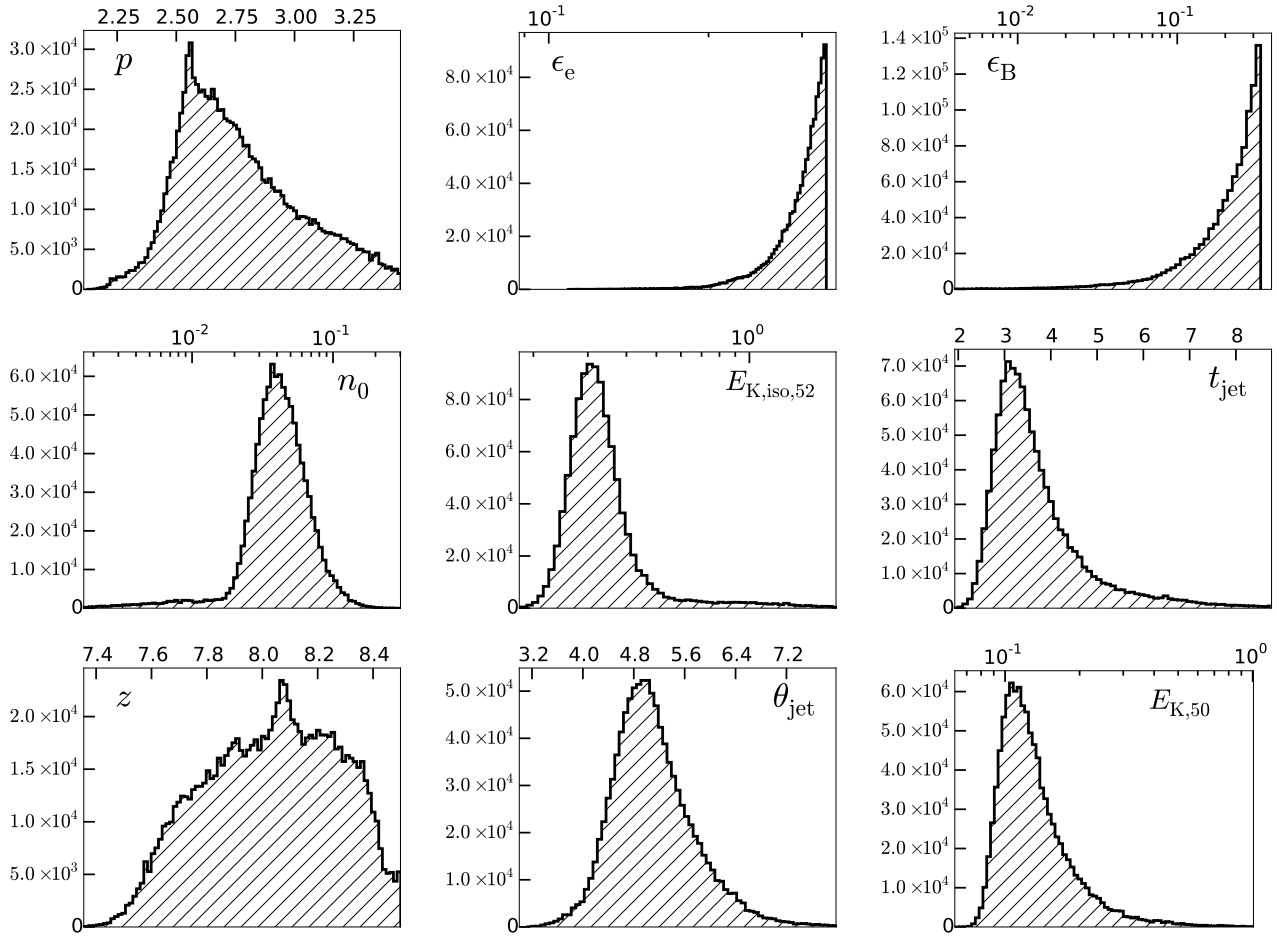

Figure 14. Posterior probability density functions for the physical parameters of GRB 120923A in the ISM-like model from MCMC simulations. We have restricted $\epsilon_e < 1/3$ and $\epsilon_B < 1/3$. Units of the quantities are: n_0 in cm^{-3}, $E_{K,iso}$ and E_K in erg, t_{jet} in days, and θ_{jet} in degrees.

for GRB afterglows thus far, it is consistent with being drawn from the same distribution.

For the beaming corrected kinetic energy, we once again work with the logarithm: $\varepsilon \equiv \log_{10}(E_K/10^{50}\,\mathrm{erg})$ and have $\bar{\varepsilon} = 0.75$, $\sigma_\varepsilon = 0.70$, and $\hat{\varepsilon} = 0.58$ for the comparison sample. For GRB 120923A, we find $\varepsilon = -0.9^{+0.16}_{-0.10}$, such that $|(\varepsilon - \bar{\varepsilon})|/\sigma_\varepsilon \approx 2.4$. Thus, although we cannot rule out that GRB 120923A is drawn from the same sample as the comparison events based on E_K, the measured value of the beaming-corrected kinetic energy in the case of this event is one of the lowest observed for GRB afterglows so far (Figure 16). A caveat here is that the comparison sample for which these parameters have been derived consists of well-studied and generally bright events, and so could itself be biased compared to the wider population.

Our *HST* observations enabled us to measure the steep light curve decay which we have attributed to a jet break. Although the identification of jet breaks in GRB afterglow light curves has sometimes proven controversial in the *Swift* era (e.g., Curran et al. 2008), the sharp and marked break in this case is rather hard to interpret otherwise. Through multi-wavelength modelling, we have derived a jet opening angle of $\theta_{jet} = 5.0^{+1.3}_{-0.8}$ degrees, the fourth such measurement at $z \gtrsim 6$. Interestingly, this value is comparable to the values obtained for other $z \gtrsim 6$ events, but is smaller than the median value for $z \sim 1$ events reported in the literature (Figure 17; although we caution that limited data for many older bursts in this compilation means that interpretation of temporal breaks as being due to beaming is less secure). This supports the hypothesis of Laskar et al. (2014) that observed high-redshift GRBs may be more tightly-beamed on the average than their more local counterparts, which may be a consequence of narrower jets leading to more intrinsically luminous and hence easier to observe afterglows. Multi-wavelength analysis for more high-redshift events coupled with a uniform statistical study of the $z \sim 1$ events would further clarify this inference.

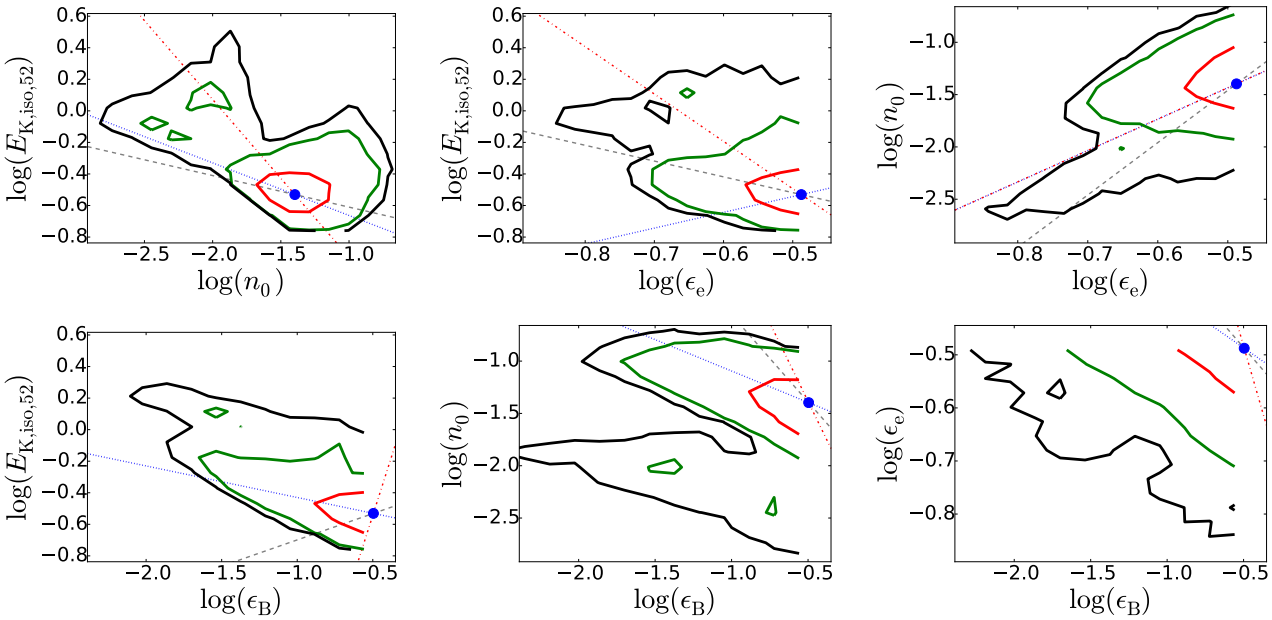

Figure 15. 1σ (red), 2σ (green), and 3σ (black) contours for correlations between the physical parameters, $E_{\rm K,iso}$, n_0, $\epsilon_{\rm e}$, and ϵ_B for GRB 120923A, in the ISM-like model from Markov chain Monte Carlo simulations. We have restricted $\epsilon_{\rm e} < 1/3$ and $\epsilon_{\rm B} < 1/3$. The lines indicate the expected relations between these parameters when $\nu_{\rm a}$ (grey, dashed), $\nu_{\rm c}$ (blue, dotted), or $\nu_{\rm m}$ (red, dash-dot) are not fully constrained, and are provided for reference, normalized to pass through the highest-likelihood point (blue dot).

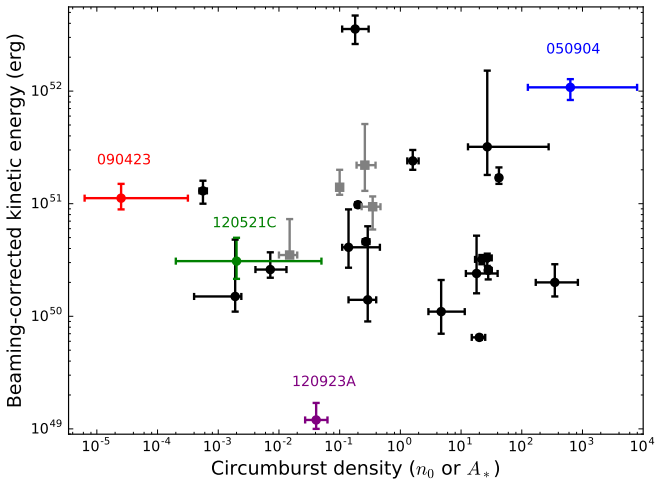

Figure 16. Beaming-corrected kinetic energy as a function of circumburst density in units of cm^{-3} from multi-wavelength modelling of GRB afterglows for both ISM (black circles) and wind-like environments (grey squares) at $z \sim 1$ (grey and black; Panaitescu & Kumar 2002; Yost et al. 2003; Chandra et al. 2008; Cenko et al. 2010, 2011; Laskar et al. 2015) and at $z \gtrsim 6$ (blue: GRB 050904, red: GRB 090423A, green: GRB 120521C, and purple: GRB 120923A; from Laskar et al. 2014 and this work).

7. CONCLUSIONS

We have presented X-ray, NIR, and radio observations of GRB 120923A. The faintness of the afterglow made the initial identification as an optical drop-out and subsequent spectroscopy challenging. Nonetheless, we were able to derive a redshift for the event of $z = 7.84^{+0.06}_{-0.12}$ from a low signal-to-noise VLT/X-shooter spectrum, which is consistent with that obtained from the photometric redshift analysis. The absence of significant flux at the afterglow location in our final *HST* image suggests the host galaxy is likely fainter than $M_{\rm F140W,AB} \gtrsim 27.5$, consistent with the deep limits on other $z \sim 8$ GRB hosts (Tanvir et al. 2012).

Our multi-wavelength modelling of all available afterglow observations, shows that a standard external shock in a constant-density circumburst environment with $n_0 \approx 0.04\,{\rm cm}^{-3}$ explains the data well. Using deep *HST* observations, we find evidence for a jet break at $t_{\rm jet} = 3.4^{+1.1}_{-0.5}$ days, from which we computed a jet opening angle of $\theta_{\rm jet} = 5.0^{+1.3}_{-0.8}$ degrees. Our results support the apparent trend of smaller opening angles for $z \gtrsim 6$ GRBs compared to $z \sim 1$ events. This may reflect the fact that at high redshift we can only detect events with the highest isotropic luminosities, which would therefore favour selection of more narrowly beamed jets assuming a fixed range of intrinsic energy reservoirs. The blastwave kinetic energy, $E_{\rm K} = 1.2^{+0.5}_{-0.2} \times 10^{49}$ erg, is one of the lowest seen so far for both nearby and high-z well-studied events. Otherwise the properties of GRB 120923A, like those of the other $z \gtrsim 6$ bursts discovered to date (Laskar et al. 2014), show no signatures

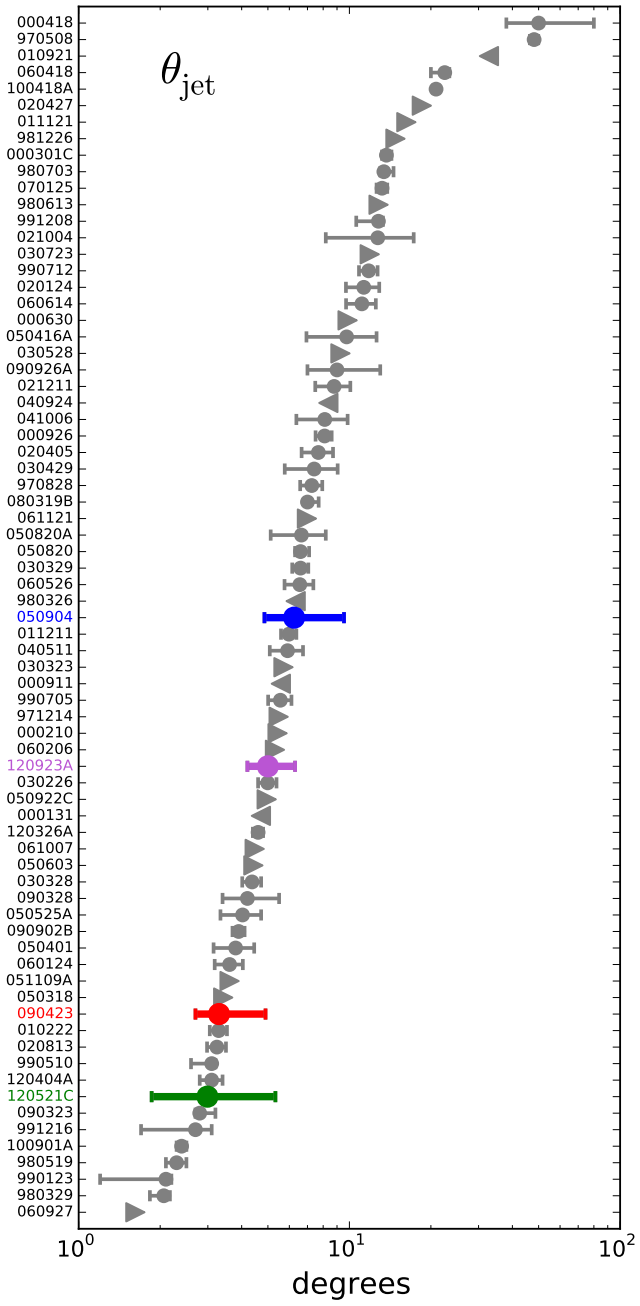

Figure 17. Jet opening angles from multi-wavelength modelling of GRB afterglows at $z \sim 1$ (grey; Friedman & Bloom 2005; Ghirlanda at al. 2007; Cenko et al. 2010, 2011; Laskar et al. 2015) and at $z \gtrsim 6$ (blue: GRB 050904, red: GRB 090423A, green: GRB 120521C, and purple: GRB 120923A; from Laskar et al. 2014 and this work).

that would suggest they could be produced by Pop III stars, such as very long duration or extremely large energy (cf. Mészáros & Rees 2010).

In the case of GRB 120923A, NIR observations within the first hours post-burst alerted us to the high-redshift nature of this event. In addition, they were essential to catch the peak of the afterglow SED at a time that the radiation was in the fast cooling regime, allowing us to constrain the circumburst density even in the absence of a radio detection and the resulting freedom in locating the synchrotron self-absorption frequency. Rapid-response NIR observations at large telescopes are therefore crucial not only for their ability to help us identify GRBs at $z \gtrsim 6$, but also for studying the progenitors and environments of these energetic phenomena, establishing them as unique probes of star-formation at the highest redshifts. In the *JWST* era, NIR spectroscopy, even several days post-burst, of similar events will provide much higher signal-to-noise data, allowing meaningful constraints to be placed on abundances and neutral hydrogen in the host galaxy.

We thank the anonymous referee for their constructive comments.

This work is based on observations made with the NASA/ESA Hubble Space Telescope, obtained at the Space Telescope Science Institute, which is operated by the Association of Universities for Research in Astronomy, Inc., under NASA contract NAS 5-26555. These observations are associated with program GO12558. Support for Program number GO12558 was provided by NASA through a grant from the Space Telescope Science Institute, which is operated by the Association of Universities for Research in Astronomy, Incorporated, under NASA contract NAS5-26555.

This work is based on observations collected at the European Organisation for Astronomical Research in the Southern Hemisphere (ESO), Chile under programme 089.A-0067, and on observations obtained at the Gemini Observatory (acquired through the Gemini Science Archive and processed using the Gemini IRAF package), which is operated by the Association of Universities for Research in Astronomy, Inc., under a cooperative agreement with the NSF on behalf of the Gemini partnership: the National Science Foundation (United States), the National Research Council (Canada), CONICYT (Chile), the Australian Research Council (Australia), Ministério da Ciência, Tecnologia e Inovação (Brazil) and Ministerio de Ciencia, Tecnología e Innovación Productiva (Argentina). The National Radio Astronomy Observatory is a facility of the National Science Foundation operated under cooperative agreement by Associated Universities, Inc.

When the data reported here were acquired, UKIRT was operated by the Joint Astronomy Centre on behalf of the Science and Technology Facilities Council of the

U.K. We thank Tim Carroll for his assistance in making these observations.

Based on data obtained with the VLA under program 12A-394. The National Radio Astronomy Observatory is a facility of the National Science Foundation operated under cooperative agreement by Associated Universities, Inc.

The Dark Cosmology Centre was funded by the DNRF. The research leading to these results has received funding from the European Research Council under the European Union's Seventh Framework Program (FP7/2007-2013)/ERC Grant agreement no. EGGS-278202.

DAK is grateful to TLS for financial support.

ERS acknowledges support from UK STFC consolidated grant ST/L000733/1

DM thanks the Instrument Center for Danish Astrophysics (IDA) for support.

AdUP acknowledges support from a Ramón y Cajal fellowship.

RSR and AdUP acknowledge support from a 2016 BBVA Foundation Grant for Researchers and Cultural Creators.

DAK, ZC, RSR and AdUP acknowledge support from the Spanish research project AYA 2014-58381-P.

DX acknowledges the support by the One-Hundred-Talent Program of the Chinese Academy of Sciences (CAS), by the Strategic Priority Research Program Multi-wavelength Gravitational Wave Universe of the CAS (No. XDB23000000), and by the National Natural Science Foundation of China under grant 11533003.

TK acknowledges support through the Sofja Kovalevskaja Award to Patricia Schady from the Alexander von Humboldt Foundation of Germany.

NRT and KW acknowledge support from the UK STFC under consolidated grant ST/N000757/1.

Facility: Gemini-North (GMOS, NIRI),

Facility: HST (WFC3-IR),

Facility: VLT (X-shooter, ISAAC, FORS2),

Facility: UKIRT (WFCAM),

Facility: VLA

REFERENCES

Barkana, R., & Loeb, A. 2004, ApJ, 601, 64

Barthelmy, S. D., Barbier, L. M., Cummings, J. R., et al. 2005, SSRv, 120, 143

Boër, M., Atteia, J. L., Damerdji, Y., et al. 2006, ApJL, 638, L71

Bolton, J. S., & Haehnelt, M. G. 2013, MNRAS, 429, 1695

Bouwens, R. J., Illingworth, G. D., Oesch, P. A., et al. 2015, ApJ, 811, 140

Bunker, A. J., Caruana, J., Wilkins, S. M., et al. 2013, MNRAS, 430, 3314

Burrows, D. N., Hill, J. E., Nousek, J. A., et al. 2005, SSRv, 120, 165

Cenko, S. B., Frail, D. A., Harrison, F. A., et al. 2010, ApJ, 711, 641

Cenko, S. B.; Frail, D. A.; Harrison, F. A., et al. 2011, ApJ, 732, 29

Chandra, P., Cenko, S. B., Frail, D. A., et al. 2008, ApJ, 683, 924

Chornock R., Berger E., Fox D. B., Fong W., Laskar T., Roth K. C., 2014, arXiv:1405.7400

Cucchiara, A., Levan, A. J., Fox, D. B., et al. 2011, ApJ, 736, 7

Curran, P. A., van der Horst, A. J., & Wijers, R. A. M. J. 2008, MNRAS, 386, 859

Curran, P. A., Evans, P. A., de Pasquale, M., Page, M. J., & van der Horst, A. J. 2010, ApJL, 716, L135

Evans, P. A., Beardmore, A. P., Page, K. L., et al. 2007, A&A, 469, 379

Evans, P. A., Beardmore, A. P., Page, K. L., et al. 2009, MNRAS, 397, 1177

Foreman-Mackey, D., Hogg, D. W., Lang, D. & Goodman, J. 2013, PASP, 125, 306

Frebel, A., & Norris, J. E. 2015, ARA&A, 53, 631

Friedman, A. S. & Bloom, J. S. 2005, ApJ, 627, 1

Fynbo, J. P. U., Jakobsson, P.; Prochaska, J. X., et al. 2009, ApJS, 185, 526

Ghirlanda, G., Nava, L., Ghisellini, G., et al. 2007, A&A, 466, 127

Goldoni, P. 2011, Astronomische Nachrichten, 332, 227

Graham, J. F., & Fruchter, A. S. 2017, ApJ, 834, 170

Granot, J., & Sari, R. 2002, ApJ, 568, 820

Granot, J., Königl, A., & Piran, T. 2006, MNRAS, 370, 1946

Greiner, J., Bornemann, W., Clemens, C., et al. 2008, PASP, 120, 405

Greiner, J., Krühler, T., Fynbo, J. P. U., et al. 2009, ApJ, 693, 1610

Greiner, J., Krühler, T., Klose, S., et al. 2011, A&A, 526, A30

Haislip, J. B., Nysewander, M. C., Reichart, D. E., et al. 2006, Nature, 440, 181
Hartoog O. E., et al., 2015, A&A, 580, 139
Hjorth, J., Sollerman, J., Møller, P., et al. 2003, Nature, 423, 847
Hjorth, J., Malesani, D., Jakobsson, P., et al. 2012, ApJ, 756, 187
Jakobsson, P., Hjorth, J., Malesani, D., et al. 2012, ApJ, 752, 62
Kann, D. A., Klose, S., Zhang, B., et al. 2010, ApJ, 720, 1513
Kawai, N., Kosugi, G., Aoki, K., et al. 2006, Nature, 440, 184
Krühler, T., Malesani, D., Milvang-Jensen, B., et al. 2012, ApJ, 758, 46
Krühler, T., Malesani, D., Fynbo, J. P. U., et al. 2015, A&A, 581, A125
Laskar, T., Berger, E., Tanvir, N., et al. 2014, ApJ, 781, 1
Laskar, T., Berger, E., Margutti, R., et al. 2015, ApJ, 814, 1
Levan, A. J., Perley, D. A., Tanvir, N. R., & Cucchiara, A. 2012, GRB Coordinates Network, 13802
Lien, A., Sakamoto, T., Gehrels, N., et al. 2014, ApJ, 783, 24
Lien, A., Sakamoto, T., Barthelmy, S. D., et al. 2016, ApJ, 829, 7
Littlejohns, O. M., Tanvir, N. R., Willingale, R., et al. 2013, MNRAS, 436, 3640
Madau, P. 1995, ApJ, 441, 18
Markwardt, C. B., Barthelmy, S. D., Baumgartner, W. H., et al. 2012, GRB Coordinates Network, 13807
Maselli, A., Melandri, A., Nava, L., et al. 2014, Science, 343, 48
McGuire, J. T. W., Tanvir, N. R., Levan, A. J., et al. 2016, ApJ, 825, 135
Melandri, A., Bernardini, M. G., D'Avanzo, P., et al. 2015, A&A, 581, A86
Mészáros P., Rees M. J., 2010, ApJ, 715, 967
Miralda-Escudé, J. 1998, ApJ, 501, 15
Oesch, P. A., Brammer, G., van Dokkum, P. G., et al. 2016, ApJ, 819, 129
Panaitescu, A., & Kumar, P., 2002, ApJ, 571, 779
Pei, Y. C. 1992, ApJ, 395, 130
Perley, D. A., Levan, A. J., Tanvir, N. R., et al. 2013, ApJ, 778, 128
Perley, D. A., Tanvir, N. R., Hjorth, J., et al. 2016, ApJ, 817, 8
Planck Collaboration, 2016, A&A, 596, A108
Racusin, J. L., Karpov, S. V., Sokolowski, M., et al. 2008, Nature, 455, 183 bibitem[Robertson et al.(2015)]Robertson15 Robertson, B. E., Ellis, R. S., Furlanetto, S. R., & Dunlop, J. S. 2015, ApJL, 802, L19
Sakamoto, T., Barthelmy, S. D., Baumgartner, W. H., et al. 2011, ApJS, 195, 2
Salvaterra, R., Della Valle, M., Campana, S., et al. 2009, Nature, 461, 1258
Sari, R., Piran, T., & Narayan, R. 1998, ApJL, 497, L17
Sari, R., Piran, T., & Halpern, J. P. 1999 ApJL, 519, L17
Schady, P., Dwelly, T., Page, M. J., et al. 2012, A&A, 537, A15
Schlafly, E. F., & Finkbeiner, D. P. 2011, ApJ, 737, 103
Starling, R. L. C., Willingale, R., Tanvir, N. R., et al. 2013, MNRAS, 431, 3159
Tanvir, N. R., & Jakobsson, P. 2007, Royal Society of London Philosophical Transactions Series A, 365, 1377
Tanvir, N. R., Fox, D. B., Levan, A. J., et al. 2009, Nature, 461, 1254
Tanvir, N. R., Levan, A. J., Fruchter, A. S., et al. 2012, ApJ, 754, 46
Thöne, C. C., Fynbo, J. P. U., Goldoni, P., et al. 2013, MNRAS, 428, 3590
Totani, T., Kawai, N., Kosugi, G., et al. 2006, PASJ, 58, 485
Trenti, M., Perna, R., Levesque, E. M., Shull, J. M., & Stocke, J. T. 2012, ApJL, 749, L38
Vergani, S. D., Salvaterra, R., Japelj, J., et al. 2015, A&A, 581, A102
Vernet, J., Dekker, H., D'Odorico, S., et al. 2011, A&A, 536, A105
Watson, D., Christensen, L., Knudsen, K. K., et al. 2015, Nature, 519, 327
Willingale, R., Starling, R. L. C., Beardmore, A. P., Tanvir, N. R., & O'Brien, P. T. 2013, MNRAS, 431, 394
Xu D., et al., 2013, ApJ, 776, 98
Yershov, V. N., Barthelmy, S. D., Krimm, H. A., et al. 2012, GRB Coordinates Network, 13796
Yost, S. A., Harrison, F. A., Sari, R., et al. 2003, ApJ, 597, 459
Zafar, T., Watson, D. J., Tanvir, N. R., et al. 2011, ApJ, 735, 2
Zhang B., et al., 2007, ApJ, 655, 989
Zhang, B., Zhang, B.-B., Virgili, F. J., et al. 2009, ApJ, 703, 1696
Zitrin, A., Labbé, I., Belli, S., et al. 2015, ApJL, 810, L12